

Evidence for dissociation and ionization of warm dense nitrogen with laser-driven shock compression to 800 GPa

Y. J. Kim, B. Militzer, B. Boates, S. Bonev, P. M. Celliers, G. W. Collins, K. P. Driver, D. E. Fratanduono, S. Hamel, R. Jeanloz, J. R. Rygg, D. C. Swift, J. H. Eggert, M. Millot

November 22, 2021

Physical review letters

Disclaimer

This document was prepared as an account of work sponsored by an agency of the United States government. Neither the United States government nor Lawrence Livermore National Security, LLC, nor any of their employees makes any warranty, expressed or implied, or assumes any legal liability or responsibility for the accuracy, completeness, or usefulness of any information, apparatus, product, or process disclosed, or represents that its use would not infringe privately owned rights. Reference herein to any specific commercial product, process, or service by trade name, trademark, manufacturer, or otherwise does not necessarily constitute or imply its endorsement, recommendation, or favoring by the United States government or Lawrence Livermore National Security, LLC. The views and opinions of authors expressed herein do not necessarily state or reflect those of the United States government or Lawrence Livermore National Security, LLC, and shall not be used for advertising or product endorsement purposes.

Evidence for dissociation and ionization in shock compressed nitrogen to 800 GPa

Yong-Jae Kim, 1, * Burkhard Militzer, 2 Brian Boates, 1 Stanimir Bonev, 1 Peter M. Celliers, 1 Gilbert W. Collins, 3 Kevin P. Driver, 1 Dayne E. Fratanduono, 1 Sebastien Hamel, 1 Raymond Jeanloz, 2 J. Ryan Rygg, 3 Damian C. Swift, 1 Jon H. Eggert, 1 and Marius Millot 1, †

1 Lawrence Livermore National Laboratory, Livermore, CA 94550, USA

2 Departments of Earth and Planetary Science and Astronomy,

University of California, Berkeley, CA 94720, USA

3 Departments of Mechanical Engineering, Physics and Astronomy,

and the Laboratory for Laser Energetics, University of Rochester, Rochester, NY 14623.

(Dated: May 14, 2022)

Abstract

Triple bonding in the nitrogen molecule (N_2) is among the strongest chemical bonds with a dissociation enthalpy of 9.8 eV/molecule. Nitrogen is therefore an excellent testbed for theoretical and numerical methods aimed at understanding how bonding evolves under the influence of the extreme pressures and temperatures of the warm dense matter regime. Here, we report laser-driven shock experiments on fluid molecular nitrogen up to 800 GPa and 4.0 g/cm³. Line-imaging VISAR velocimetry and impedance matching with a quartz reference yield shock equation of state data of initially precompressed nitrogen. Comparison with numerical simulations using path integral Monte Carlo and density functional theory molecular dynamics (PIMC-DFTMD) reveals clear signatures of chemical dissociation and the onset of L-shell ionization. Combining data along multiple shock Hugoniot curves starting from densities between 0.76 to 1.29 g/cm³, our study documents how pressure and density affect these changes in chemical bonding, and provides benchmarks for future theoretical developments in this regime, with applications for planetary interior modeling, high energy density science, and inertial confinement fusion research.

Elemental nitrogen (Z=7) forms diatomic N_2 molecules with extremely strong triple covalent bonds (9.8 eV/molecule) at 300 K and 1 bar. This unique bonding yields not only stability and chemical inertia, but also a diverse solid-state polymorphism over a wide range of pressure-temperature conditions. The gradual evolution of chemical bonding and molecular/atomic rearrangements under elevated pressure and temperature are of great interest, as nitrogen is expected to be present in icy planet interiors [1, 2], is also an important detonation product [3, 4], and is critical to many energetic materials [5]. For example, static compression studies of this simple molecular system using diamond anvil cells (DACs) at low and moderate temperature have revealed more than 15 solid phases differing by subtle re-arrangements of the nitrogen molecules driven by pressure-induced symmetric breaking [6–8], or the weakening and breaking of the triple bonds to form single-bonded polymeric phases [9–11].

Upon increasing temperature well above $1000 \,\mathrm{K}$, molecular fluid nitrogen has been predicted to transform into an atomic fluid, a polymeric fluid, and a strongly coupled plasma [12–16]. Therefore, this prototypical low-Z molecular system is an excellent test bed for the development of advanced numerical and theoretical approaches for matter in the high energy density (HED) regime [17] and inertial confinement fusion (ICF) science [18]. For example, recent experiments have shown that the shock density of deuterium (D_2) near $400\text{-}1,000 \,\mathrm{GPa}$ along a double shock path, starting from the cryogenic liquid, cannot be reconciled with predictions from density functional theory molecular dynamics (DFTMD) and broad-range equation of state (EOS) models [19]. Having a heavier atomic nucleus, nitrogen's properties may be easier to capture with current quantum simulation techniques. We expect a negligible quantum zero-point motion, a reliable Born-Oppenheimer approximation, and an accurate classical description of ion dynamics in DFTMD for nitrogen at high pressure and temperature conditions [15]. Studying nitrogen might therefore help to unlock some of the mysteries regarding the behavior of hydrogen in the warm dense regime—with important implications for ICF science—by providing a means to compare theoretical and numerical approaches with experimental data for bonding changes and ionization of a low-Z diatomic molecule in the absence of the key complexities that arise when dealing with H atoms.

While various other low-Z materials have been studied under extreme conditions using dynamic compression experiments [17, 20–23], there are few experimental results to compare with simulations for nitrogen above 100 GPa [24, 25]. Most shock compression experiments on molecular nitrogen have been performed on the cryogenic fluid with initial density ρ_{LN} of 0.81 g/cm³ (at 77 K) with planar impactors [25–32] up to 80 GPa. These revealed the onset of molecular dissociation into an atomic fluid at 30 GPa and 2.3-fold compression by comparing with a theoretical molecular Hugoniot [30, 33], and evidence of its completion at 80 GPa and 3.7-fold compression [30, 32] in agreement with DFTMD simulations [15]. The only available shock EOS data in the multimegabar regime, obtained with hemispherical-shell impacts, reported an isochoric compression at 4.2-fold compression between 100 and 320 GPa. This was interpreted as evidence for a polymeric fluid state [24, 25] and supported by average-atom simulations [14], but appears to be in stark

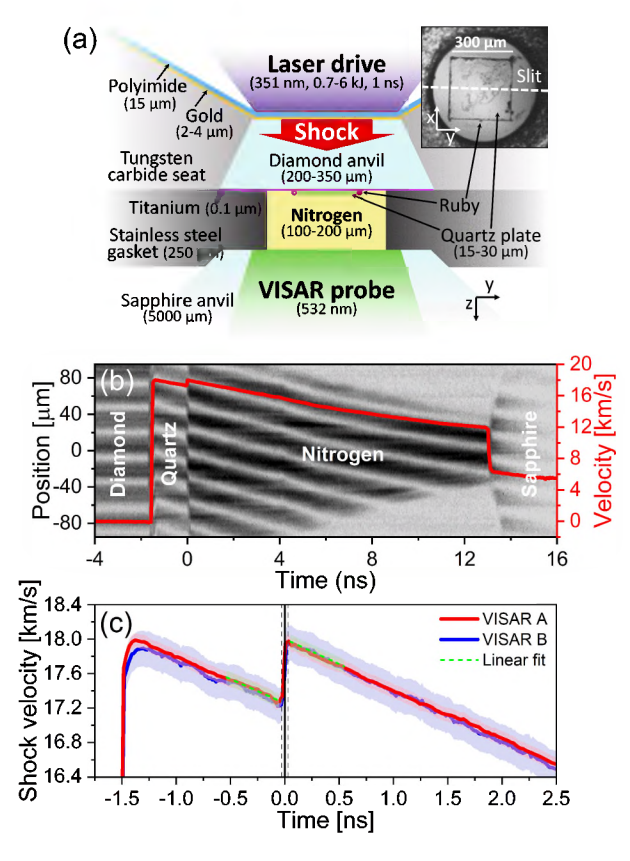


Figure 1. (a) Sketch of the experimental configuration including the diamond/sapphire anvil cell target, the focus locations of the laser-drive beams and Doppler velocimetry (VISAR) probe. Inset micrograph shows the pressure chamber containing transparent molecular nitrogen fluid, a quartz reference plate, and ruby pressure markers. The white dashed line represents the projection of the VISAR streak camera entrance slit onto the target. (b) Raw image for shot 65143, overlaid with the corresponding shock-front velocity history (red). (c) Velocity profiles for shot 65143 measured with the two VISAR channels (A and B), and the linear fitting and extrapolation of the higher-resolution velocity channel to the impedance match event (set as $t_{IM} = 0$ s, black vertical line). Shaded area represents the systematic uncertainty for each channel. Black dotted vertical lines indicate the timing uncertainty for this event.

disagreement with the DFTMD simulations.

In this study, we performed laser-driven shock experiments on fluid molecular nitrogen precompressed in diamond/sapphire anvil cells to provide new experimental data in the range of this discrepancy between experiments and quantum simulations. Doppler velocimetry and impedance matching with a quartz reference were used to document the shock pressure-density EOS of nitrogen up to 800 GPa, 2.5 times higher pressure than those of previous studies [24]. The behavior observed in our new data is well captured by DFTMD simulations, and reveals clear signatures of the chemical dissociation of molecular nitrogen into an atomic fluid and the onset of L-shell ionization across a wide range of pressure-density-temperature conditions.

The precompressed laser-shock targets were prepared using diamond/sapphire anvil cells (see Fig. 1a and Supplemental Materials [34]). Liquid nitrogen was loaded cryogenically into the high-pressure cell, then compressed at room temperature to an initial pressure (P_0) of 0.23-2.03 GPa, measured by ruby

luminescence [45]. The density (ρ_0) and refractive index (n_0) of the pre-shot sample were inferred as 0.76-1.29 g/cm³ and 1.18-1.32, respectively, based on previous studies [46–50], and are listed in Table S1 [34].

We conducted 21 shock experiments on the Omega Laser Facility at the University of Rochester (NY, USA). We used up to 12 beams with 23 or 48° incident angles to deliver 0.7-6.0 kJ of 351 nm UV laser in a 1 ns super-Gaussian flat-top pulse with a \sim 0.1 ns 10%-90% rise time. Phase plates (SG8 with a 438 µm radius at e^{-1} maximum intensity and a 4.5 super-Gaussian exponent, and E-SG-865 with 430 and 396 µm major and minor radii and a 4.7 super-Gaussian exponent) were used to produce a flat-top laser intensity distribution matching the 900 µm diameter opening on the drive side of the diamond anvil.

In the experiments described here, the initially transparent quartz and nitrogen become optically reflective under shock compression, so that the shock front can be directly tracked with a line-imaging velocity interferometer system for any reflector (VISAR). We record two VISAR channels (A and B) with 18.23 and 7.212 mm thick etalons, giving a vacuum velocity per fringe (VPF) of 2.732 and 6.906 km/s/fringe: with distinct values of VPF, the two VISAR records allow us to confirm the magnitudes of fringe offsets at each interface. In Fig. 1b, the shock wave arrives at the diamond-quartz interface (\sim -2 ns), breaks out of the quartz into the sample (t_{IM} =0 ns), and transits through the nitrogen layer before entering the sapphire anvil (\sim 18.5 ns). The stationary VISAR signal before -2 ns originates from the laser probe reflecting off the Ti mirror coating on the diamond.

Standard phase unwrapping and correction using the refractive indices $n_0(P_0)$ of the precompressed quartz and nitrogen yield the shock-front velocity history $U_S(t)$ shown in Fig. 1b and 1c: $U_S = U_{app}/n_0$, where U_{app} is the apparent shock velocity [22, 51, 52]. We determine the shock velocities of the quartz $(U_{S,Q})$ and nitrogen sample (U_S) at their interface (t_{IM}) using the VISAR signal with the highest precision (i.e., VISAR A), by linearly fitting the velocity over 0.5-1.0 ns and extrapolating the fits to t_{IM} , as shown in Fig.1c. For each shot, we estimate the uncertainty of the phase retrieval by determining the value needed to get the error bars of the velocity traces from the two VISAR channels to overlap, which is found as 3-5% of the VPF. From the jump in shock velocity between the incident shock in quartz and the transmitted shock in nitrogen, we determine how compressible nitrogen is relative to quartz with the impedance matching technique (see Supplemental Materials [34] and related Refs. [53-55]). The measured shock velocities of quartz and nitrogen $(U_{S,Q})$ and U_{S} and inferred shock states of nitrogen (u_p, P, ρ, ρ) and ρ/ρ_0 for each shot are summarized in Table S2 [34]. Error propagation including random and systematic errors is carried out using a Monte-Carlo methodology with the Cholesky decomposition to generate correlated random variables from the covariance matrices of the various model parameters [22, 34].

In order to compare with our experiments, shock Hugoniot curves are computed for five different initial densities including the cryogenic liquid density (0.81 g/cm³), 0.91, 1.08, 1.16, and 1.27 g/cm³ from the first-principles equation of state described in Refs. [15, 56]. Depending on the temperature, these simulations use either DFTMD with the Perdew-Burke-Ernzerhof exchange-correlation functional in the generalized gradient

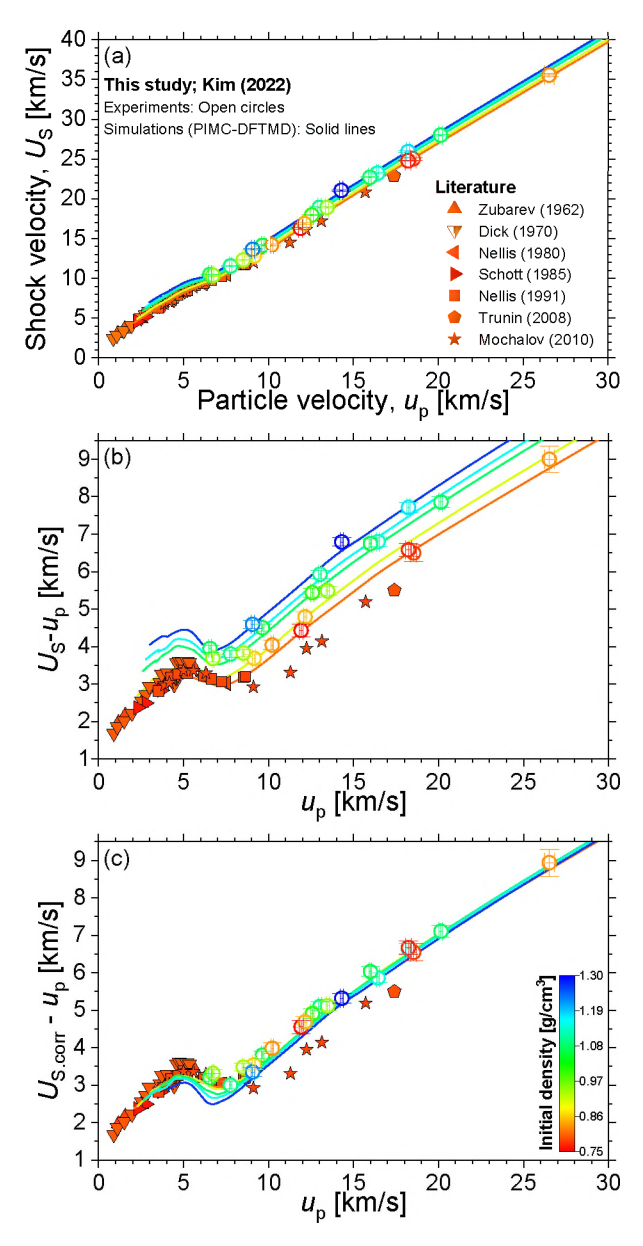


Figure 2. Shock velocity versus particle velocity of nitrogen. (a) Our data extend the previously explored range [24–30]. (b) Showing the data in the U_S-u_p vs u_p plane reveals non-linearity and initial density trends. (c) Shock velocities for various initial densities are corrected to match those for liquid nitrogen density, further enhancing the evidence for subtle changes in shock compression, and providing a basis for detailed comparison with the corresponding Hugoniot curves derived from PIMC-DFTMD simulations [solid curves in (a), (b), and (c)]. Color scale corresponds to the initial density of the nitrogen sample.

approximation, or path integral Monte Carlo (PIMC) methods. We computed the change in internal energy induced by the precompression, then solved the energy conservation Rankine-Hugoniot equation for specific internal energy, using a bicubic spline in density-temperature space. Along the Hugoniot curves considered here, the switch from DFTMD to PIMC occurs around 3,000 GPa. We note that the difference in internal energy between the cryogenic and precompressed fluids at $0.81g/\text{cm}^3$ ($\sim 0.06 \text{ eV/molecule}$) is much smaller than the shock-induced internal energy variation ($\sim 5-100 \text{ eV/molecule}$); see Fig. S2 and S1 [34].

The U_S versus u_p data for our 21 experiments on precompressed nitrogen are plotted in Fig. 2a and compared with the results of previous experimental studies on cryogenic liquid nitrogen [24–29, 32], including the gas-gun study up to 80 GPa by Nellis *et al.* [32] (square) and the hemi-spherical explosive experiments up to 320 GPa by Trunin *et al.* [24] and Mochalov *et al.* [25] (pentagon and star); for their initial conditions, see Table S3 [34]. We also plot a series of simulated Hugoniot curves with various ρ_0 (with density as a color scale). Our dataset extends over a broad range of U_S , from 10.3 to 35.5 km/s, which is 1.5 times higher than previous results [24]. On such an extended scale, all data points appear to lie broadly scattered around a single line regardless of the ρ_0 .

Plotting $U_S - u_p$ as a function of u_p on Fig. 2b helps to visualize non-linearity and initial density trends better [57]. In this plot, our lowest velocity data appear to overlap with the bulk of the data points from previous studies on cryogenic liquid nitrogen. In addition, U_S clearly scales with ρ_0 as observed previously in D₂ [53], He [58], CO₂ [23], SiO₂ [54], and porous metals [59]. Indeed, a shift in U_S proportional to ρ_0 is found to collapse all experimental data into a single line, allowing us to compare directly Hugoniot data with various initial states (Fig. 2c and Fig. S3 [34]).

We found that the Hugoniot curves simulated with the PIMC-DFTMD methods agree with current and previous experimental data over a wide velocity range, except for the data from Refs. [24] and [25] which will be discussed later (Fig. 2b). Both experimental and simulated data show two abrupt slope changes (i.e., softening and stiffening) near $u_p = 5$ and 8 km/s (Fig. S4 [34]). These are interpreted as signatures of the compression changes associated with the onset and completion of the shock-induced dissociation of the nitrogen molecules [24, 25, 30, 32]. When the simulated U_S are corrected to account for their ρ_0 , they overlap well before ($u_p < 5$ km/s) and after (>8 km/s) the chemical dissociation region (Fig. 2c). The extensive velocity overlap in the experiments and simulations confirms that the compressibility of different ρ_0 data are similar, despite the fact that our data span different P-T- ρ conditions. In other words, the bonding changes appear as smooth, rather than sharp transitions. However, a closer look at the family of simulated Hugoniot curves in the dissociation regime ($5 < u_p < 8$ km/s) suggests that the transition becomes sharper with increasing ρ_0 , i.e. at lower temperature, as illustrated by the predicted dissociation boundary [13, 15] which becomes a first-order transition at lower temperature and higher pressure (Fig. S5 [34]).

The P- ρ values of our low- ρ_0 data (ρ_0 =0.76-0.87 g/cm³) are plotted in Fig. 3a, along with previous experimental data and various simulation curves for cryogenic liquid nitrogen. Our data range is 101-798 GPa and 2.78-3.38 g/cm³, with a maximum compression of 4.18-fold over the liquid nitrogen density. We find that pressure increases from 100 GPa to 400 GPa almost isochorically near 2.8-3.0 g/cm³, corresponding to ρ/ρ_{LN} =3.5-3.7. Above 400 GPa, shocked nitrogen reaches higher compression with increasing P up to our maximum pressure level of 800 GPa.

The Hugoniot curves derived from the simulations reproduce the behavior observed in the experimental data over a wide P- ρ range (10-800 GPa and 1.5-3.4 g/cm³), and capture the slope changes near 30, 80, and

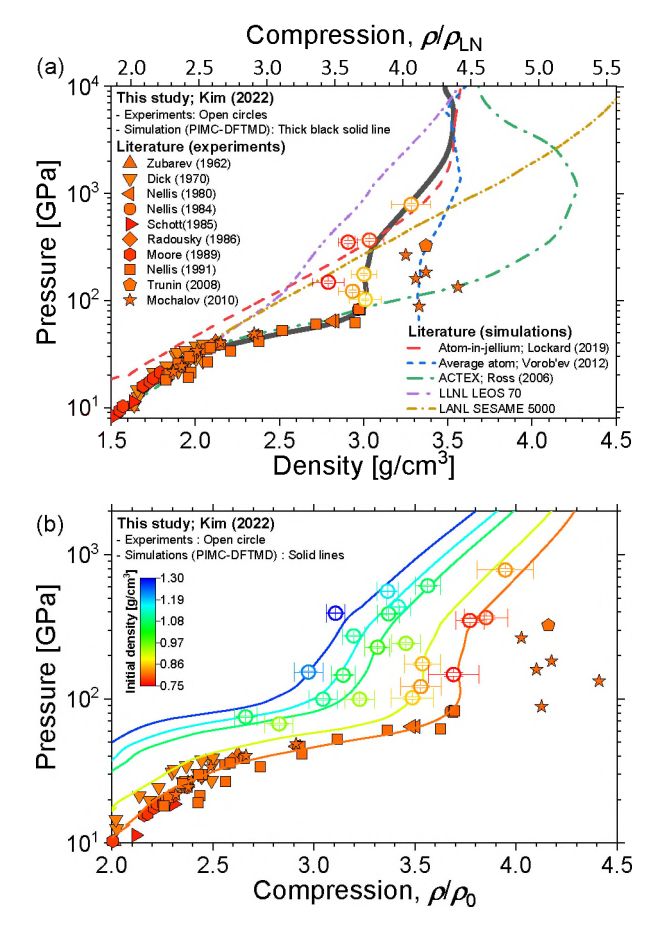


Figure 3. Shock pressure versus density of nitrogen. (a) Comparison of experimental data in this (ρ_0 =0.76–0.87 g/cm³) and previous [24–30, 32, 60, 61] studies with simulated Hugoniot curves using various models [12, 14–16] for cryogenic liquid nitrogen. (b) Our experimental data for a wide range of initial densities (ρ_0 =0.76–1.29 g/cm³) is well described by the simulated Hugoniot curves. A common color scale representing the nitrogen sample's initial density is used for both experimental data and simulated Hugoniot curves.

400 GPa quite well (Fig. 3a). The two slope changes at lower pressures (i.e., softening and stiffening) are interpreted as signatures of the onset and completion of the chemical dissociation [30, 32], as discussed above for Fig. 2b. Consistently, the stiff behavior in the 100-400 GPa range apparent in our experimental data suggests that molecular dissociation is largely completed by ~100 GPa. Our simulation shows a compression maximum beyond the pressure level experimentally explored in this study (> 800 GPa), corresponding to complete L-shell ionization at 4,000 GPa, 3.5 g/cm³, and 4.3-fold compression [15]. This suggests the increased compressibility observed above 400 GPa can be related to the onset of L-shell ionization of the dissociated atomic nitrogen.

We note that the previous data from hemispherical compressions [24, 25] (pentagon and star) are slower (Fig. 2b) and denser (Fig. 3a) in the dissociated atomic regime, as compared with our experimental and simulation results. This discrepancy remains unexplained, but could arise from the neglect of 2D and possibly 3D effects in the analysis of those experiments which rely on hydrodynamic simulations to account for the

shock's spherical convergence and acceleration. In addition, the reported uncertainty in the measured shock velocity in Ref. [25] ($\Delta U_S/U_S$ =1.8-3.3 %) is much larger than in our experiments ($\Delta U_S/U_S$ =0.1-0.7 %); for a further discussion, see Supplemental Materials [34].

Our experimental and simulation results are also compared with predictions from various numerical and theoretical methods in Fig. 3a. First, the less computationally demanding atom-in-jellium approach [16] compares well with our data after the softening at 400 GPa. However, this model cannot capture chemical bonding, so it is inadequate in the molecular, dissociation, and atomic regimes. Next, the average-atom model [14] describes the isochoric compression and ionization-induced softening in a similar pressure regime as our results. However, as it reproduces the results by Trunin *et al.* [24] and Mochalov *et al.* [25] at higher density, this model is in disagreement with ours. The ACTEX simulation curve [12] extrapolated below 2,000 GPa to match the gas-gun data at 20-80 GPa is found to be inconsistent with our results. Finally, both the molecular vibration-based (SESAME 5000) and Thomas-Fermi (LEOS 70) models match experimental data very well below 30 GPa, but are inadequate above that shock pressure as they lack a description of the molecular dissociation and ionization phenomena. The SESAME 5000 approaches a maximum compression ratio of 6 (as expected for a perfect diatomic gas with the heat capacity ratio γ of 7/5 [62]), while the LEOS 70 exhibits a peak compression (not shown here) at a similar density but higher pressure than the L-shell ionization in the PIMC-DFTMD simulations.

Our complete experimental P versus ρ/ρ_0 dataset ($\rho_0 = 0.76$ -1.29 g/cm³) is shown in Fig. 3b. While the precompression allows us to reach denser shock states than the principal Hugoniot of cryogenic liquid nitrogen, and explore more extreme conditions of density for this material reaching 4.0 g/cm³ (Fig. S8 [34]), we find that the shock compression ratio (ρ/ρ_0) is reduced with increasing precompression and initial density. This could be interpreted as being due to stronger particle interactions (which decrease the compression) at higher shock density and reduced excitation of internal degrees of freedom, such as molecular dissociation and thermal ionization (which increases the compression) for shock compression of an initially denser sample [15, 58].

A closer look at our experimental data compared with the corresponding simulation curves (matching colors on Fig. 3b) provides further confidence in the ability of the DFTMD simulations to accurately capture the subtle changes in material properties at these previously undocumented conditions. Along the precompressed Hugoniot curves with $\rho_0 > 0.81$ g/cm³, no stiff isochoric behavior is observed between 100 and 400 GPa. Rather, the compressibility in this pressure range increases gradually with ρ_0 . This behavior is opposite to that expected for increased particle interactions, but implies that the excitation process becomes more important at lower pressures with increasing ρ_0 . For a further understanding of nitrogen's behavior in the Mbar regime, we computed the electronic density of states with DFTMD simulations (Fig. S9) at various pressures (107-735 GPa) for a 3.706 g/cm³ density (Figs. S5 and S8), showing that more L-shell electrons become excited above the Fermi energy with increasing pressure. This electronic excitation increases the

internal energy, which leads to an increase in shock compression, as is discussed by Militzer [63]. Therefore, we reach the conclusion that the enhanced compression above 400 GPa, or 14 km/s in u_p (Fig. 2c and S6 [34]), can be understood as being due to L-shell ionization enhancing the compressibility of dissociated nitrogen.

Although the current experimental study with a kJ laser drive covers only the initiation of L-shell ionization at low pressures, recent measurements in spherical geometry [17] using a MJ laser drive at the National Ignition Facility (NIF) clearly documented signatures of K-shell ionization of carbon in the 15-45 TPa range and could be used for future experiments on nitrogen. In addition, on-going development of a new DAC platform on NIF is paving the way to investigate equally interesting phenomena at much lower temperature such as the early observation of shock cooling [31] and the later prediction of a first-order transition between molecular fluid and polymeric fluid [15]. Altogether, the development of EOS measurement techniques opens novel opportunities to unravel matter's response to extreme conditions (e.g., dissociation, ionization, and electron degeneracy), enabling a better understanding of dense celestial objects such as white dwarfs and exoplanets.

Acknowledgement

This work was prepared by LLNL under contract DE-AC52-07NA27344 and was supported by LLNL LDRD program 19-ERD-031. Partial funding for G.W.C. and J.R.R. was provided by NSF Physics Frontier Center award PHY-2020249. We acknowledge technical assistance from Eric Folsom, Renee Posadas, Carol Davis and Jim Emig. The data in this work were analyzed with LLNL AnalyzeVISAR code.

^{*} kim100@llnl.gov

[†] millot1@llnl.gov

^[1] W. B. Hubbard, Science **214**, 145 (1981).

^[2] K. Soderlund, M. Bethkenhagen, I. de Pater, J. Fortney, S. Hamel, R. Helled, Y.-J. Kim, M. Millot, and S. Stanley, Bulletin of the AAS 53, 20190479 (2021).

^[3] M. Bagge-Hansen, S. Bastea, J. A. Hammons, M. H. Nielsen, L. M. Lauderbach, R. L. Hodgin, P. Pagoria, C. May, S. Aloni, A. Jones, W. L. Shaw, E. V. Bukovsky, N. Sinclair, R. L. Gustavsen, E. B. Watkins, B. J. Jensen, D. M. Dattelbaum, M. A. Firestone, R. C. Huber, B. S. Ringstrand, J. R. I. Lee, T. van Buuren, L. E. Fried, and T. M. Willey, Nature Communications 10, 3819 (2019).

^[4] M. C. Marshall, A. Fernandez-Pañella, T. W. Myers, J. H. Eggert, D. J. Erskine, S. Bastea, L. E. Fried, and L. D. Leininger, Journal of Applied Physics 127, 185901 (2020).

^[5] D. Badgujar, M. Talawar, S. Asthana, and P. Mahulikar, Journal of Hazardous Materials 151, 289 (2008).

^[6] H. Katzke and P. Tolédano, Physical Review B 78, 064103 (2008).

- [7] A. Erba, L. Maschio, C. Pisani, and S. Casassa, Physical Review B 84, 012101 (2011).
- [8] R. Turnbull, M. Hanfland, J. Binns, M. Martinez-Canales, M. Frost, M. Marqués, R. T. Howie, and E. Gregoryanz, Nature Communications 9, 4717 (2018).
- [9] C. Mailhiot, L. H. Yang, and A. K. McMahan, Physical Review B 46, 14419 (1992).
- [10] M. I. Eremets, A. G. Gavriliuk, I. a. Trojan, D. a. Dzivenko, and R. Boehler, Nature Materials 3, 558 (2004).
- [11] C. Ji, A. A. Adeleke, L. Yang, B. Wan, H. Gou, Y. Yao, B. Li, Y. Meng, J. S. Smith, V. B. Prakapenka, W. Liu, G. Shen, W. L. Mao, and H.-k. Mao, Science Advances 6, eaba9206 (2020).
- [12] M. Ross and F. Rogers, Physical Review B 74, 024103 (2006).
- [13] B. Boates and S. A. Bonev, Physical Review Letters 102, 1 (2009).
- [14] V. S. Vorob'ev, A. S. Grushin, and V. G. Novikov, The Journal of Chemical Physics 137, 031102 (2012).
- [15] K. P. Driver and B. Militzer, Physical Review B 93, 064101 (2016).
- [16] T. Lockard, M. Millot, B. Militzer, S. Hamel, L. X. Benedict, P. A. Sterne, and D. C. Swift, Atom-in-jellium equations of state for cryogenic liquids, Tech. Rep. (2020) arXiv:1906.09516v2.
- [17] A. L. Kritcher, D. C. Swift, T. Döppner, B. Bachmann, L. X. Benedict, G. W. Collins, J. L. DuBois, F. Elsner, G. Fontaine, J. A. Gaffney, S. Hamel, A. Lazicki, W. R. Johnson, N. Kostinski, D. Kraus, M. J. MacDonald, B. Maddox, M. E. Martin, P. Neumayer, A. Nikroo, J. Nilsen, B. A. Remington, D. Saumon, P. A. Sterne, W. Sweet, A. A. Correa, H. D. Whitley, R. W. Falcone, and S. H. Glenzer, Nature 584, 51 (2020).
- [18] S. Le Pape, L. F. Berzak Hopkins, L. Divol, A. Pak, E. L. Dewald, S. Bhandarkar, L. R. Bennedetti, T. Bunn, J. Biener, J. Crippen, D. Casey, D. Edgell, D. N. Fittinghoff, M. Gatu-Johnson, C. Goyon, S. Haan, R. Hatarik, M. Havre, D. D.-m. Ho, N. Izumi, J. Jaquez, S. F. Khan, G. A. Kyrala, T. Ma, A. J. Mackinnon, A. G. MacPhee, B. J. MacGowan, N. B. Meezan, J. Milovich, M. Millot, P. Michel, S. R. Nagel, A. Nikroo, P. Patel, J. Ralph, J. S. Ross, N. G. Rice, D. Strozzi, M. Stadermann, P. Volegov, C. Yeamans, C. Weber, C. Wild, D. Callahan, and O. A. Hurricane, Physical Review Letters 120, 245003 (2018).
- [19] A. Fernandez-Pañella, M. Millot, D. E. Fratanduono, M. P. Desjarlais, S. Hamel, M. C. Marshall, D. J. Erskine, P. A. Sterne, S. Haan, T. R. Boehly, G. W. Collins, J. H. Eggert, and P. M. Celliers, Physical Review Letters 122, 255702 (2019).
- [20] P. M. Celliers, G. W. Collins, D. G. Hicks, M. Koenig, E. Henry, A. Benuzzi-Mounaix, D. Batani, D. K. Bradley, L. B. Da Silva, R. J. Wallace, S. J. Moon, J. H. Eggert, K. K. M. Lee, L. R. Benedetti, R. Jeanloz, I. Masclet, N. Dague, B. Marchet, M. Rabec Le Gloahec, C. Reverdin, J. Pasley, O. Willi, D. Neely, and C. Danson, Physics of Plasmas 11, L41 (2004).
- [21] P. Loubeyre, S. Brygoo, J. Eggert, P. M. Celliers, D. K. Spaulding, J. R. Rygg, T. R. Boehly, G. W. Collins, and R. Jeanloz, Physical Review B 86, 144115 (2012).
- [22] M. Millot, S. Hamel, J. R. Rygg, P. M. Celliers, G. W. Collins, F. Coppari, D. E. Fratanduono, R. Jeanloz, D. C. Swift, and J. H. Eggert, Nature Physics 14, 297 (2018).
- [23] L. E. Crandall, J. R. Rygg, D. K. Spaulding, T. R. Boehly, S. Brygoo, P. M. Celliers, J. H. Eggert, D. E. Fratanduono, B. J. Henderson, M. F. Huff, R. Jeanloz, A. Lazicki, M. C. Marshall, D. N. Polsin, M. Zaghoo, M. Millot, and G. W. Collins, Physical Review Letters 125, 165701 (2020).
- [24] R. F. Trunin, G. V. Boriskov, A. I. Bykov, A. B. Medvedev, G. V. Simakov, and A. N. Shuikin, JETP Letters 88, 189 (2008).
- [25] M. A. Mochalov, M. V. Zhernokletov, R. I. Il'kaev, A. L. Mikhailov, V. E. Fortov, V. K. Gryaznov, I. L. Iosilevskiy, A. B. Mezhevov, A. E. Kovalev, S. I. Kirshanov, Y. A. Grigor'eva, M. G. Novikov, and A. N. Shuikin, Journal

- of Experimental and Theoretical Physics 110, 67 (2010).
- [26] V. Zubarev, Dokl. Akad. Nauk SSSR 142, 309 (1962).
- [27] R. D. Dick, The Journal of Chemical Physics **52**, 6021 (1970).
- [28] G. L. Schott, M. S. Shaw, and J. D. Johnson, The Journal of Chemical Physics 82, 4264 (1985).
- [29] W. J. Nellis and A. C. Mitchell, The Journal of Chemical Physics 73, 6137 (1980).
- [30] W. J. Nellis, N. C. Holmes, A. C. Mitchell, and M. van Thiel, Physical Review Letters 53, 1661 (1984).
- [31] H. B. Radousky and M. Ross, High Pressure Research 1, 39 (1988).
- [32] W. J. Nellis, H. B. Radousky, D. C. Hamilton, A. C. Mitchell, N. C. Holmes, K. B. Christianson, and M. van Thiel, The Journal of Chemical Physics 94, 2244 (1991).
- [33] M. Ross and F. H. Ree, The Journal of Chemical Physics 73, 6146 (1980).
- [34] See Supplemental Material at [URL] for more details, which includes Refs. [35–44].
- [35] G. Ghosh, Dispersion-equation coefficients for the refractive index and birefringence of calcite and quartz crystals, Optics Communications 163, 95 (1999).
- [36] E. Calderon, M. Gauthier, F. Decremps, G. Hamel, G. Syfosse, and A. Polian, Complete determination of the elastic moduli of α-quartz under hydrostatic pressure up to 1 GPa: an ultrasonic study, Journal of Physics: Condensed Matter 19, 436228 (2007).
- [37] H. Kimizuka, S. Ogata, J. Li, and Y. Shibutani, Complete set of elastic constants of α-quartz at high pressure: A first-principles study, Physical Review B 75, 054109 (2007).
- [38] J. C. Chervin, B. Canny, and M. Mancinelli, Ruby-spheres as pressure gauge for optically transparent high pressure cells, High Pressure Research 21, 305 (2001).
- [39] W. J. Moonan, Linear Transformation to a Set of Stochastically Dependent Normal Variables, Journal of the American Statistical Association 52, 247 (1957).
- [40] R. Y. Rubinstein and D. P. Kroese, Simulation and the Monte Carlo Method, 3rd ed. (John Wiley & Sons, Inc., 2016).
- [41] A.-L. Cholesky, Sur la résolution numérique des systèmes d'équations linéaires, Bulletin de la Sabix, 81 (2005).
- [42] J. Sun, M. Martinez-Canales, D. D. Klug, C. J. Pickard, and R. J. Needs, Stable All-Nitrogen Metallic Salt at Terapascal Pressures, Physical Review Letters 111, 175502 (2013).
- [43] R. Chau, A. C. Mitchell, R. W. Minich, and W. J. Nellis, Metallization of Fluid Nitrogen and the Mott Transition in Highly Compressed Low-Z Fluids, Physical Review Letters 90, 245501 (2003).
- [44] P. M. Celliers, G. W. Collins, D. G. Hicks, and J. H. Eggert, Systematic uncertainties in shock-wave impedance-match analysis and the high-pressure equation of state of Al, Journal of Applied Physics 98, 113529 (2005).
- [45] H. K. Mao, J. Xu, and P. M. Bell, Journal of Geophysical Research 91, 4673 (1986).
- [46] R. L. Mills, D. H. Liebenberg, and J. C. Bronson, The Journal of Chemical Physics 63, 1198 (1975).
- [47] D. Fabre and B. Oksengorn, Applied Spectroscopy 46, 468 (1992).
- [48] H. D. Hochheimer, K. Weishaupt, and M. Takesada, The Journal of Chemical Physics 105, 374 (1996).
- [49] S. Jiang, N. Holtgrewe, S. S. Lobanov, F. Su, M. F. Mahmood, R. S. McWilliams, and A. F. Goncharov, Nature Communications 9, 2624 (2018).
- [50] S. Ninet, G. Weck, A. Dewaele, F. Datchi, V. M. Giordano, and P. Loubeyre, The Journal of Chemical Physics 153, 114503 (2020).
- [51] P. M. Celliers, D. K. Bradley, G. W. Collins, D. G. Hicks, T. R. Boehly, and W. J. Armstrong, Review of Scientific Instruments 75, 4916 (2004).

- [52] Y.-J. Kim, P. M. Celliers, J. H. Eggert, A. Lazicki, and M. Millot, Scientific Reports 11, 5610 (2021).
- [53] D. G. Hicks, T. R. Boehly, P. M. Celliers, J. H. Eggert, S. J. Moon, D. D. Meyerhofer, and G. W. Collins, Physical Review B 79, 014112 (2009).
- [54] S. Brygoo, M. Millot, P. Loubeyre, A. E. Lazicki, S. Hamel, T. Qi, P. M. Celliers, F. Coppari, J. H. Eggert, D. E. Fratanduono, D. G. Hicks, J. R. Rygg, R. F. Smith, D. C. Swift, G. W. Collins, and R. Jeanloz, Journal of Applied Physics 118, 195901 (2015).
- [55] M. P. Desjarlais, M. D. Knudson, and K. R. Cochrane, Journal of Applied Physics 122, 035903 (2017).
- [56] B. Militzer, F. González-Cataldo, S. Zhang, K. P. Driver, and F. Soubiran, Physical Review E 103, 013203 (2021).
- [57] G. I. Kerley, "The linear U_S - u_P relation in shock-wave physics," (2006), arXiv:1306.6916v3.
- [58] J. Eggert, S. Brygoo, P. Loubeyre, R. S. McWilliams, P. M. Celliers, D. G. Hicks, T. R. Boehly, R. Jeanloz, and G. W. Collins, Physical Review Letters 100, 124503 (2008).
- [59] R. F. Trunin, Physics Uspekhi 44, 371 (2001).
- [60] H. B. Radousky, W. J. Nellis, M. Ross, D. C. Hamilton, and A. C. Mitchell, Physical Review Letters 57, 2419 (1986).
- [61] D. S. Moore, S. C. Schmidt, M. S. Shaw, and J. D. Johnson, The Journal of Chemical Physics 90, 1368 (1989).
- [62] Y. B. Zeldovich and Y. P. Raizer, Physics of Shock Waves and High-Temperature Hydrodynamic Phenomena (Elsevier, 1967).
- [63] B. Militzer, Physical Review Letters 97, 175501 (2006).

Supplemental Materials

Evidence for dissociation and ionization in shock compressed nitrogen to 800 GPa

Yong-Jae Kim,^{1,*} Burkhard Militzer,² Brian Boates,¹ Stanimir Bonev,¹ Peter M. Celliers,¹ Gilbert W. Collins,³ Kevin P. Driver,¹ Dayne E. Fratanduono,¹ Sebastien Hamel,¹ Raymond Jeanloz,² J. Ryan Rygg,³ Damian C. Swift,¹ Jon H. Eggert,¹ and Marius Millot^{1,†}

¹Lawrence Livermore National Laboratory, Livermore, CA 94550, USA ²Departments of Earth and Planetary Science and Astronomy, University of California, Berkeley, CA 94720, USA

³Departments of Mechanical Engineering, Physics and Astronomy, and the Laboratory for Laser Energetics, University of Rochester, Rochester, NY 14623. (Dated: May 14, 2022)

^{*} kim100@llnl.gov

[†] millot1@llnl.gov

Table S1. Density and refractive index of the quartz reference ($\rho_{0.Q}$ and $n_{0.Q}$) and nitrogen sample (ρ_0 and n_0) at the initial pressure (P_0) and room temperature (296 K) for each shot. These initial properties are inferred based on previous studies; Ref. [S1–S4] for quartz and Ref. [S5–S9] for nitrogen. The uncertainty in P_0 is 0.03 GPa.

Shot	D [CDa]	Qua	artz	Nitro	itrogen	
number	$P_0 \; [\mathrm{GPa}]$	$ ho_{0.Q}~[{ m g/cm^3}]$	$n_{0.Q}$	$ ho_0 \; [{ m g/cm^3}]$	$\overline{n_0}$	
64352	1.35	2.739 ± 0.004	1.560 ± 0.001	1.177 ± 0.008	1.288 ± 0.003	
64354	1.16	2.727 ± 0.003	$1.558 \pm \ 0.001$	1.136 ± 0.009	1.277 ± 0.003	
64358	2.03	2.780 ± 0.005	1.566 ± 0.001	1.294 ± 0.006	1.317 ± 0.003	
64359	0.23	2.665 ± 0.002	1.549 ± 0.001	0.756 ± 0.029	1.180 ± 0.007	
65132	0.27	2.668 ± 0.002	1.550 ± 0.001	0.788 ± 0.025	1.188 ± 0.007	
65135	0.93	2.712 ± 0.003	1.556 ± 0.001	1.078 ± 0.010	1.263 ± 0.003	
65139	0.92	2.711 ± 0.003	1.556 ± 0.001	1.075 ± 0.010	1.262 ± 0.003	
65140	0.55	2.687 ± 0.002	1.552 ± 0.001	0.948 ± 0.014	1.229 ± 0.004	
65141	1.02	2.718 ± 0.003	1.557 ± 0.001	1.102 ± 0.009	1.269 ± 0.003	
65142	0.87	2.708 ± 0.003	1.555 ± 0.001	1.061 ± 0.010	1.258 ± 0.003	
65143	0.69	2.696 ± 0.003	1.554 ± 0.001	1.003 ± 0.012	1.243 ± 0.003	
65144	0.89	2.709 ± 0.003	1.556 ± 0.001	1.066 ± 0.010	1.260 ± 0.003	
65145	0.25	2.666 ± 0.002	1.549 ± 0.001	0.771 ± 0.027	1.184 ± 0.007	
66035	0.38	2.675 ± 0.002	1.551 ± 0.001	0.863 ± 0.019	1.207 ± 0.005	
66036	0.99	2.716 ± 0.003	1.557 ± 0.001	1.094 ± 0.010	1.267 ± 0.003	
66037	0.55	2.687 ± 0.002	1.552 ± 0.001	0.948 ± 0.014	1.229 ± 0.004	
66055	0.53	2.686 ± 0.002	1.552 ± 0.001	0.940 ± 0.015	1.227 ± 0.004	
66059	0.33	2.672 ± 0.002	1.550 ± 0.001	0.832 ± 0.021	1.199 ± 0.006	
66485	0.33	2.672 ± 0.002	1.550 ± 0.001	0.832 ± 0.021	1.199 ± 0.006	
68045	1.62	2.755 ± 0.004	1.562 ± 0.001	1.228 ± 0.007	1.300 ± 0.003	
68049	0.36	2.674 ± 0.002	1.550 ± 0.001	0.849 ± 0.020	1.204 ± 0.005	

Table S2. Shock velocity $(U_{S,Q})$ of the quartz reference, and the shock and particle velocities $(U_S \text{ and } u_p)$ and shock pressure and density $(P \text{ and } \rho)$ of the nitrogen sample for each shot at the time of the impedance match event (t_{IM}) . ρ_0 in Table. S1 is duplicated in the table below, showing how the shock compression ratio (ρ/ρ_0) is calculated. These shock parameters are evaluated at the quartz-nitrogen interface through the typical VISAR analysis method [S10–S12] and impedance matching technique [S4, S13]. The temperatures were not measured but calculated from the first-principles equation of state (FPEOS) database [S14] (T_{DFT}) by constructing theoretical shock Hugoniot curves for the different initial densities and matching the experimentally determined pressure. The error bars on T_{DFT} were obtained by propagating the uncertainties in the pressure and initial densities.

Shot	Quartz			Nitr	ogen			
number	$U_{S.Q} \; [{ m km/s}]$	$U_S \; [{ m km/s}]$	$u_p \; [\mathrm{km/s}]$	P [GPa]	$ ho~[{ m g/cm}^3]$	$ ho_0 \ [{ m g/cm}^3]$	$ ho/ ho_0$	$T_{DFT} \; [m kK]$
64352	23.75±0.06	25.95±0.09	18.24 ± 0.10	558.2 ± 4.2	3.96 ± 0.06	1.177 ± 0.008	3.37 ± 0.05	68.14 ± 0.64
64354	21.71±0.06	23.24 ± 0.09	16.44 ± 0.09	435.0 ± 3.6	$3.88 {\pm} 0.07$	1.136 ± 0.009	$3.42 {\pm} 0.06$	$56.52 {\pm} 0.65$
64358	19.98±0.06	21.10 ± 0.08	14.31 ± 0.08	392.6 ± 2.7	4.02 ± 0.06	1.294 ± 0.006	3.11 ± 0.05	$43.51 {\pm} 0.45$
64359	15.75±0.06	16.35 ± 0.12	11.92 ± 0.12	147.6 ± 4.6	2.79 ± 0.09	$0.756 {\pm} 0.029$	3.69 ± 0.13	31.04 ± 1.84
65132	22.45 ± 0.06	25.03 ± 0.16	18.53 ± 0.16	365.7 ± 9.2	3.03 ± 0.09	$0.788 {\pm} 0.025$	3.83 ± 0.11	68.87 ± 2.37
65135	25.29 ± 0.06	28.00 ± 0.09	20.14 ± 0.11	608.7 ± 5.4	$3.84 {\pm} 0.06$	1.078 ± 0.010	$3.56 {\pm} 0.06$	79.63 ± 0.88
65139	10.56 ± 0.06	10.51 ± 0.07	$6.56 {\pm} 0.06$	75.1 ± 0.9	$2.86 {\pm} 0.06$	1.075 ± 0.010	$2.66 {\pm} 0.06$	$6.37 {\pm} 0.15$
65140	10.51 ± 0.06	10.41 ± 0.07	6.73 ± 0.06	67.0 ± 1.1	$2.68 \pm \ 0.07$	$0.948 {\pm} 0.014$	$2.83 {\pm} 0.07$	7.27 ± 0.26
65141	18.01±0.06	18.96 ± 0.08	13.03 ± 0.08	273.1 ± 2.5	3.52 ± 0.06	1.102 ± 0.009	3.20 ± 0.05	36.73 ± 0.55
65142	14.13±0.05	14.15 ± 0.07	9.65 ± 0.06	145.7 ± 1.5	$3.34 {\pm} 0.06$	1.061 ± 0.010	3.15 ± 0.06	18.02 ± 0.43
65143	17.22±0.06	18.02 ± 0.08	12.58 ± 0.08	228.1 ± 2.6	3.32 ± 0.06	1.003 ± 0.012	3.31 ± 0.06	$34.32 {\pm} 0.71$
65144	21.04±0.06	22.74 ± 0.08	15.99 ± 0.09	388.7 ± 3.7	3.59 ± 0.06	1.066 ± 0.010	3.37 ± 0.05	$54.51 {\pm} 0.73$
65145	22.12±0.06	24.82 ± 0.02	18.24 ± 0.16	349.3 ± 9.9	$2.91 {\pm} 0.06$	0.771 ± 0.027	3.77 ± 0.07	$67.58 {\pm} 2.59$
66035	13.06±0.06	12.83 ± 0.09	9.15 ± 0.08	101.7 ± 2.0	3.01 ± 0.09	$0.863 {\pm} 0.019$	3.49 ± 0.10	$16.11 {\pm} 0.76$
66036	11.98±0.06	11.57±0.07	7.77 ± 0.06	99.3 ± 1.1	3.33 ± 0.07	1.094 ± 0.010	3.05 ± 0.07	$9.22 {\pm} 0.28$
66037	17.98±0.06	18.96 ± 0.09	13.47 ± 0.09	242.8 ± 3.3	3.28 ± 0.07	$0.948 {\pm} 0.014$	$3.46{\pm}0.07$	$39.42 {\pm} 0.89$
66055	12.54±0.05	12.34 ± 0.08	8.52 ± 0.06	99.3 ± 1.5	3.03 ± 0.07	$0.940 \pm\ 0.015$	3.23 ± 0.07	13.20 ± 0.54
66059	30.39±0.09	35.52 ± 0.20	26.52 ± 0.29	783.8 ± 17.7	3.28 ± 0.12	0.832 ± 0.021	3.95 ± 0.14	120.23±3.14
66485	14.17±0.05	14.26±0.10	10.22±0.08	$121.5\pm\ 2.8$	2.93 ± 0.08	0.832 ± 0.021	3.53 ± 0.10	21.59 ± 1.04
68045	13.82±0.08	13.65±0.07	9.06 ± 0.09	153.4 ± 1.8	3.65 ± 0.08	1.228 ± 0.007	2.91 ± 0.07	14.25 ± 0.33
68049	16.28±0.06	16.94±0.10	12.15±0.10	175.0 ± 3.5	3.00 ± 0.08	0.849 ± 0.020	3.54±0.09	32.06±1.21

Table S3. Summary of initial properties of cryogenic nitrogen sample ($P_0 = \sim 100 \text{ kPa}$) in previous studies which results are plotted in Fig. 2 and 3 in the main text.

Reference	Initial temperature [K]	Initial density [g/cm ³]
Zubarev (1962) [S15]	77.4	0.808
$Dick\ (1970)\ [S16]$	75	0.820
Nellis (1980) $[S17]$	77.5-77.7	0.807-0.808
Nellis (1984) $[S18]$	77	0.810
Schott (1985) [S19]	85.1-85.4	0.769-0.771
Radousky (1986) [S20]	77	0.808
Moore (1989) [S21]	80.7-84.3	0.776-0.792
Nellis (1991) [S22]	76.2-78.3	0.804-0.813
Trunin (2008) [S23]	77	0.810
Mochalov (2010) [S24]	77	0.807

High pressure cell

The precompressed laser-shock targets were prepared using diamond/sapphire anvil cells (Fig. 1a in the main text). Each cell had a 200-350 µm thick, laser-drive side diamond anvil with a 2-4 µm Au x-ray preheat shield covered by a 15 µm polyimide ablator deposited on its outer surface. The drive-side sample interface had a 100 nm Ti mirror coating. A 300 µm wide, 15-30 µm thick quartz plate served as the shock reference, and a few 5-10 µm diameter ruby balls [S25] were positioned around the edges of the quartz. A 500-600 µm diameter hole in a 250 µm thick stainless steel gasket defined the sample chamber. A 5,000 µm thick sapphire anvil served as a window on the diagnostics side of the sample. Both sapphire and quartz had anti-reflection (AR) coatings to avoid spurious reflections of the VISAR laser probe.

Impedance matching

From the jump in shock velocity between the incident shock in quartz and the transmitted shock in nitrogen (Fig. 1c in the main text), we determine how compressible nitrogen is relative to quartz with the impedance matching technique [S4, S13]. To do this, we utilize a previously established relationship between shock and particle velocities for initially precompressed quartz [S4], the momentum conservation Rankine-Hugoniot equation $P = P_0 + \rho_0 U_S u_p$ [S26], and the measured $U_{S,Q}$ to determine the pressure (P) and particle velocity (u_p) of the incident shock. Then, we use an analytical model to describe the quartz isentropic release from this incident shock state [S27], and obtain the pressure and particle velocity of the transmitted shock by invoking the continuity of these quantities at the quartz/nitrogen interface and using once again the momentum conservation equation, this time, for a shock in the nitrogen sample. The density (ρ) and compression ratio (ρ/ρ_0) of the shocked sample are calculated with the mass conservation Rankine-Hugoniot equation; $\rho = \rho_0 U_S/(U_S - u_p)$. And the shock-induced variation in the internal energy $(E - E_0)$ is calculated using the energy conservation Rankine-Hugoniot equation (Fig. S1); $E - E_0 = \frac{1}{2}(P - P_0)(\frac{1}{\rho_0} - \frac{1}{\rho})$.

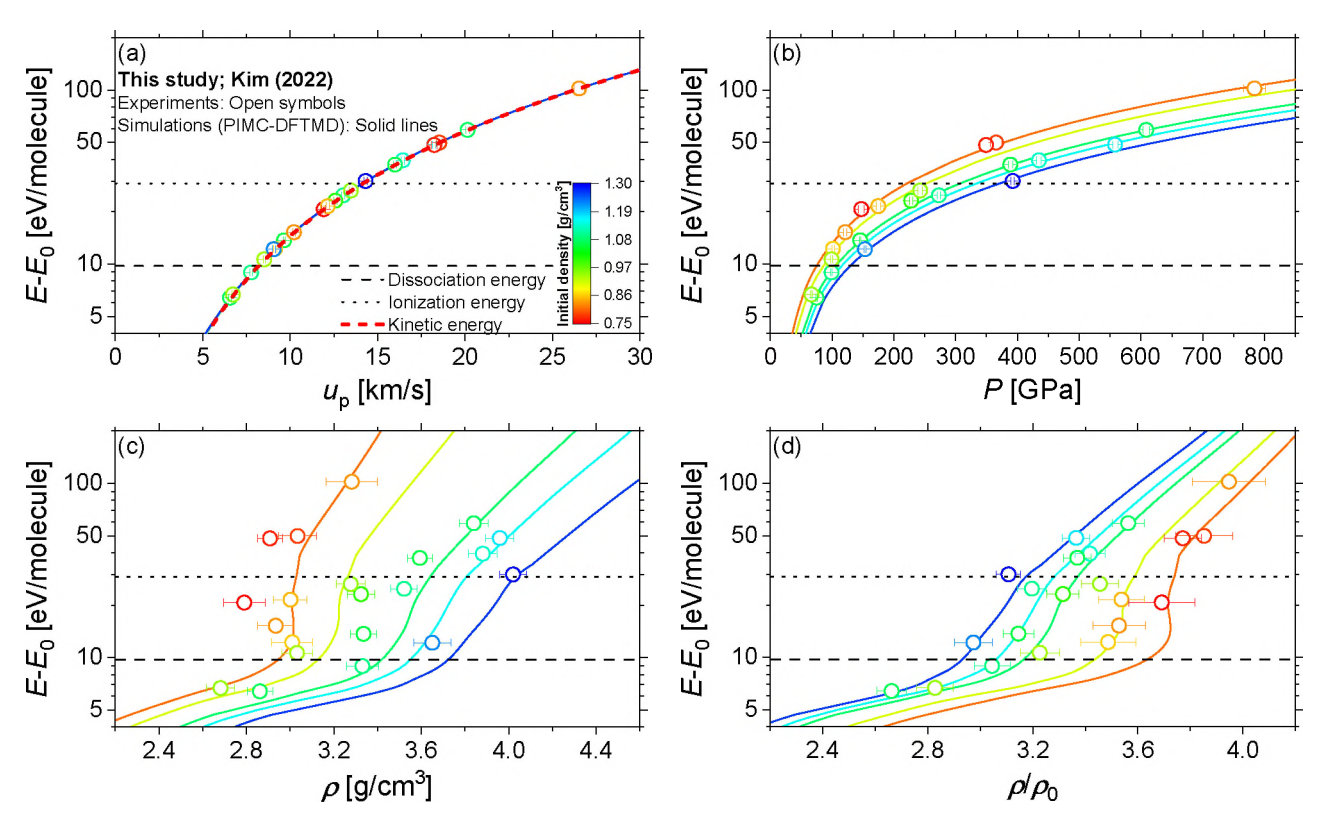


Figure S1. The shock-induced variation in the internal energy $(E-E_0)$ is calculated using the energy conservation Rankine-Hugoniot equation $[E-E_0=\frac{1}{2}(P-P_0)(\frac{1}{\rho_0}-\frac{1}{\rho})]$ in the unit of eV per N_2 molecule, and plotted as a function of the (a) particle velocity u_p , (b) pressure P, (c) density ρ , and (d) compression ratio ρ/ρ_0 of the shocked nitrogen sample. Molecular dissociation energy $(E_d=9.75 \text{ eV/molecule}, \text{ horizontal black dashed line})$ and atomic ionization energy $(E_i=14.53 \text{ eV/atom}=29.06 \text{ eV/molecule}, \text{ horizontal black dotted line})$ are shown in (a)-(d). Kinetic energy of nitrogen molecule $(E_k=\frac{1}{2}m_{N_2}u_p^2)$, where m_{N_2} is the molar mass of molecular nitrogen, thick red dashed curve) is also drawn in (a).

Error propagation

Impedance matching technique and Rankine-Hugoniot relations are used to determine shock parameters $(u_p, P, \rho, \text{ and } E-E_0)$ with known initial properties (P_0, ρ_0, n_0) and measured shock velocities (U_S) of quartz reference and nitrogen sample, and known U_S - u_p Hugoniot and Γ_{eff} - U_S release models of precompressed quartz. During these processes, a Monte-Carlo (MC) methodology with 10,000 iterations $(N_{MC} = 10,000)$ is used to compute random and systematic error propagations of the shock parameters.

Some variables $(X, \text{ such as } U_S \text{ and } P_0 \text{ of quartz and nitrogen})$ are directly measured as a mean (μ_X) and uncertainty (Δ_X) . For these variables, the random sampling is carried out from a Gaussian distribution;

$$X_{Indep} = \mu_X + G(0, \Delta_X) = G(\mu_X, \Delta_X)$$
(S1)

where X_{Indep} is the independent random sample of the variable X, and $G(\mu, \Delta)$ is the probability density function, generating a random value from a Gaussian distribution with a mean μ and standard deviation Δ . Other variables $(Y, \text{ such as } \rho_0 \text{ and } n_0 \text{ of quartz and nitrogen, and } u_p \text{ and } \Gamma_{eff} \text{ of quartz)}$ are inferred with models in literature which are functions of measurable variables X [Y = f(X) or Y(X), such as $\rho_0(P_0)$, $n_0(P_0)$, $u_p(U_S)$, and $\Gamma_{eff}(U_S)$ relations]. In this case, their independent random sample (Y_{Indep}) is calculated by solving the model with X_{Indep} from Eq. S1;

$$Y_{Indep} = f(X_{Indep}). (S2)$$

At each iteration $(i=1, 2, \dots, N_{MC})$, the obtained random variables $(X_{Indep,i} \text{ and } Y_{Indep,i})$ are used to calculate the shock parameter $(Z_{Indep,i}, \text{ such as } u_p, P, \rho, \text{ and } E - E_0)$. Then, the distribution of results $(\mathbf{Z}_{Indep} = \{Z_{Indep,1}, Z_{Indep,2}, \dots, Z_{Indep,N_{MC}}\})$ is statistically analyzed to yield a standard deviation $(\Delta_{Z_{Indep}})$ which we can use to estimate the random uncertainty (Δ_{Ran}) by setting all other uncertainty sources to zero in our MC calculation.

To evaluate how systematic uncertainties affect our experimental results, we also include uncertainties on the models of quartz Hugoniot, its initial pressure dependence, quartz release, quartz/nitrogen refractive index, and quartz/nitrogen equation of sates. If covariance matrix are available, we use the Cholesky decomposition to compute sets of correlated random variables [S28–S30]. For example, assuming a X-Y relation ($Y = a_1 + a_2X^2 + \cdots + a_NX^{N-1}$) and its covariance matrix (Σ) for the sets of parameters (a={ a_1, a_2, \dots, a_N }), we can generate sets of correlated random parameters (b={ b_1, b_2, \dots, b_N }) to perform our impedance matching calculation. In other words, this means that, instead of generating the independent random variables Y_{Indep} by using Eq. S2 with the uncorrelated parameters a, the use of the Cholesky decomposition allows us to generate sets of random parameters b that are properly correlated by Σ and dependent random variables Y_{Dep} . For completeness, we describe the simple matrix algebra behind the Cholesky decomposition below. Consider a Hermitian positive-definite N-by-N matrix, Σ for the parameters

 \boldsymbol{a} of a given model is

$$\Sigma = \begin{pmatrix} \operatorname{Cov}(a_1, a_1) & \operatorname{Cov}(a_1, a_2) & \cdots & \operatorname{Cov}(a_1, a_N) \\ \operatorname{Cov}(a_2, a_1) & \operatorname{Cov}(a_2, a_2) & \cdots & \operatorname{Cov}(a_2, a_N) \\ \vdots & \vdots & \ddots & \vdots \\ \operatorname{Cov}(a_N, a_1) & \operatorname{Cov}(a_N, a_2) & \cdots & \operatorname{Cov}(a_N, a_N) \end{pmatrix}$$
(S3)

and

$$Cov(a_i, a_j) = Exp[(a_i - Exp(a_i)(a_j - Exp(a_j))],$$
(S4)

where $Cov(a_i, a_j)$ is the covariance between two model parameters a_i and a_j , and $Exp(a_i)$ is the expected (or mean μ) value of model parameter a_i [S29]. This covariance matrix can be decomposed into the form of

$$\Sigma = L \cdot L^{T} = \begin{pmatrix} L_{1,1} & 0 & \cdots & 0 \\ L_{2,1} & L_{2,2} & \cdots & 0 \\ \vdots & \vdots & \ddots & \vdots \\ L_{N,1} & L_{N,2} & \cdots & L_{N,N} \end{pmatrix} \cdot \begin{pmatrix} L_{1,1} & L_{2,1} & \cdots & L_{N,1} \\ 0 & L_{2,2} & \cdots & L_{N,2} \\ \vdots & \vdots & \ddots & \vdots \\ 0 & 0 & \cdots & L_{N,N} \end{pmatrix}$$

$$= \begin{pmatrix} L_{1,1}^{2} & L_{2,1}L_{1,1} & \cdots & L_{N,1}L_{1,1} \\ L_{2,1}L_{1,1} & L_{2,1}^{2} + L_{2,2}^{2} & \cdots & L_{N,1}L_{2,1} + L_{N,2}L_{2,2} \\ \vdots & \vdots & \ddots & \vdots \\ L_{N,1}L_{1,1} & L_{N,1}L_{2,1} + L_{N,2}L_{2,2} & \cdots & L_{N,1}^{2} + L_{N,2}^{2} + \cdots + L_{N,N}^{2} \end{pmatrix}, \tag{S5b}$$

where L is the lower triangular matrix with positive diagonal entries, and L^T is the conjugate transpose of L. This process (Eq. S5a) is known as the Cholesky decomposition [S30], which can be computed by comparing Eqs. S3 and S5b;

$$L_{i,i} = \sqrt{\text{Cov}(a_i, a_i) - \sum_{k=1}^{i-1} L_{i,k}^2}$$

$$L_{i,j} = \frac{1}{L_{j,j}} \left[\text{Cov}(a_i, a_j) - \sum_{k=1}^{j-1} L_{i,k} L_{j,k} \right] \quad \dots \text{ for } i > j.$$
(S6)

Next, the correlated random model parameters (b) are sampled by adding dependent random values $(G(0,1)\cdot L^T)$ to the mean model parameters (a);

$$\boldsymbol{b} = \boldsymbol{a} + \boldsymbol{G}(0,1) \cdot \boldsymbol{L}^T \tag{S7}$$

where $G(\mu, \Delta)$ is a $1 \times N$ random matrix containing uncorrelated random values generated by $G(\mu, \Delta)$ similarly than for Eq. S1.

Using sets of correlated random parameters (b) to conduct the impedance matching, we can estimate the systematic uncertainty (Δ_{Sys}) on our results by setting the sources of random uncertainty to zero. Finally,

by running the Monte-Carlo with all sources of uncertainty and analyzing the statistical distribution of the results, we obtain the total uncertainty (Δ_{Tot}) reported in Table S1 and S2.

In this work, we consider the systematic contributions of n- ρ [S1, S4], P- ρ [S2, S3], U_S - u_p [S4], and Γ_{eff} - U_S [S27] models in the quartz reference. The refractive index of the precompressed quartz at 296 K is inferred with the initial quartz density [S1, S4], and used to correct a shock-front velocity history directly measured from the VISAR fringe shift ($U_S = U_{app}/n_0$ where U_{app} is the apparent shock velocity);

$$n_Q = \left(c_{11} + \frac{c_{12}\lambda^2}{\lambda^2 - c_{13}} + \frac{c_{14}\lambda^2}{\lambda^2 - c_{15}}\right)^{0.5} + 0.1461(\rho_Q - 2.649)$$
 (S8)

where the model parameters are c_{11} =1.286, c_{12} =1.070, c_{13} =0.01006 nm², c_{14} =1.102, and c_{15} =100 nm², and λ is the wavelength of VISAR laser (532 nm). Due to the absence of the parameter uncertainties and their covariance matrix and the facts that the refractive index slowly changes with density and its uncertainty is much smaller than the uncertainties of other factors (such as VPF, linear fitting of U_S -t plot, and extrapolation to t_{IM}), the dependent random variable of $n_{0,Q}$ is inferred by directly solving Eq. S8 with the dependent random variable of $\rho_{0,Q}$ which is inferred from a Murnaghan-type P- ρ equation of state at 300 K as follows;

$$\rho = 2.649 \left(P \frac{K_0'}{K_0} + 1 \right)^{1/K_0'} \tag{S9}$$

where the quartz density at ambient conditions is 2.649 g/cm^3 , and K_0 and K'_0 are the bulk modulus and its pressure derivate which are 37.5 ± 0.2 GPa and 4.7 ± 0.5 below 1 GPa [S2] and 37.7 ± 0.3 and 4.9 ± 0.1 above 1 GPa [S3]. As the covariance matrix between these model parameters (K_0 and K'_0) in Eq. S9 is not provided in literature, we approximate the statistical distribution of the parameters as uncorrelated and write each parameter as

$$b' = a + G(0, \Delta_a) = G(a, \Delta_a). \tag{S10}$$

We note that Eq. S10 likely overestimates the final uncertainty. Instead of using a Gaussian distribution above, for the K_0 and K'_0 , we use an uniform distribution between $a - \Delta_a$ and $a + \Delta_a$ to minimize computing instability;

$$b'' = a + U(0, \Delta_a) = U(a, \Delta_a). \tag{S11}$$

Then, the dependent random variables of $\rho_{0.Q}$ is inferred by computing Eq. S9 with the measured P_0 and uncorrelated random parameters (Eq. S11). Next, we use the U_S - u_p relation for quartz at ambient conditions (2.649 g/cm³) [S4] as followed;

$$U_S = \begin{cases} c_{21} + c_{22}u_p + c_{23}u_p^2, & \text{if } u_p \le c_{24}, \\ (c_{21} - c_{23}c_{24}^2) + (c_{22} + 2c_{23}c_{24})u_p, & \text{if } u_p > c_{24}. \end{cases}$$
(S12)

The model parameters are c_{21} =2.124 km/s, c_{22} =1.720 (km/s)⁻¹, c_{23} =-0.01744 (km/s)⁻², and c_{24} =14.17 km/s, and their covariance matrix is shown in Table S4 which allows us to obtain correlated random model

parameters (Eq. S7) and generate a $U_{S,Q}(\rho_0, u_p)$ relationship at ρ_0 =2.649 g/cm³. We account for the initial precompression of the quartz having a density $\rho_{0,Q}$ by adding a term $\alpha_{Corr}(\rho_0)$ to $U_{S,Q}(2.649, u_p)$;

$$\alpha_{Corr,Q} = U_{S,Corr,Q}(\rho_{0,Q}, u_p) - U_{S,Q}(2.649, u_p)$$

$$= c_{31} + c_{32}u_p(\rho_{0,Q} - 2.649)$$
(S13)

where the parameters c_{31} and c_{32} are 2.3 ± 0.4 km/s and -0.037 ± 0.027 cm³/g, respectively [S4]. Here we use uncorrelated random parameters (Eq. S11) to compute the dependent random variable of $\alpha_{Corr,Q}$. Finally, we obtain a dependent random P- u_p Hugoniot curve of the precompressed quartz by solving the momentum conservation Rankine-Hugoniot ($P = P_0 + \rho_0 U_{S,Corr} u_p$ where $U_{S,Corr} = U_S + \alpha_{Corr,Q}$) with the measured P_0 and the inferred dependent random ρ_0 , U_S , and $\alpha_{Corr,Q}$. The quartz isentropic release is obtained with the effective Grüneisen parameter Γ_{eff} model by Desjarlais et al. [S27];

$$\Gamma_{eff} = \begin{cases}
c_{41} + c_{42}U_{S,Q}, & \text{if } U_{S,Q} \le c_{43}, \\
c_{44} \left\{ 1 - \exp\left[c_{45} \left(U_{S,Q} - c_{46}\right)^{3/2}\right] \right\}, & \text{if } U_{S,Q} > c_{43}.
\end{cases}$$
(S14)

where the parameters are c_{41} =-1.4545, c_{42} =0.1102 (km/s)⁻¹, c_{43} =14.69 km/s, c_{44} =0.579, c_{45} =-0.129 (km/s)^{-2/3}, and c_{46} =-12.81 km/s. Its reported uncertainty ($\Delta\Gamma_{eff}$ =0.036) is directly used to infer the dependent random variable of Γ_{eff} by using an uniform distribution $U(\Gamma_{eff}, 0.036)$.

Similarly, the refractive index and density of the precompressed nitrogen sample are needed. We fit existing n-P data [S6–S9] as

$$n = d_{11} + d_{12}\log P + d_{13}\log^2 P + d_{14}\log^3 P$$
(S15)

where the model parameters are $d_{11}=1.267$, $d_{12}=0.1523$, $d_{13}=0.02436$, and $d_{14}=0.003102$, and their covariance matrix is summarized in Table S5. And we use a $P-\rho$ model by Mills *et al.* [S5];

$$\rho = 28.01 \left(d_{21} P^{d_{22}} T^{d_{23}} + d_{24} ln(P) + \frac{d_{25}}{P} + \frac{d_{26}}{P^2} + d_{27} \right)^{-1}$$
(S16)

where the molar mass of nitrogen molecule is 28.01 g/cm³, T is the temperature (296 K), and the model parameters are d_{21} =0.07530 (GPa^{- d_{22}}K^{- d_{23}}), d_{22} =-0.7236, d_{23} =0.7586, d_{24} =-3.171, d_{25} =-1.293 GPa, d_{26} =0.02787 GPa², and d_{27} =21.11, and their covariance matrix are summarized in Table. S6.

Table S4. The covariance matrix between the U_S - u_p model parameters of ambient density quartz in Eq. S12.

	c_{21}	c_{22}	c_{23}	c_{24}
c_{21}	1.06078×10^{-2}	-2.41829×10^{-3}	$1.26174{\times}10^{-4}$	9.85349×10^{-2}
c_{22}	-2.41829×10^{-3}	$5.76841{\times}10^{-4}$	-3.09596×10^{-5}	-2.58116×10^{-2}
c_{23}	$1.26174{\times}10^{-4}$	-3.09596×10^{-5}	$1.69748{\times}10^{-6}$	$1.49757{\times}10^{-3}$
c_{24}	9.85349×10^{-2}	-2.58116×10^{-2}	$1.49757{\times}10^{-3}$	2.02317

Table S5. The covariance matrix between the n-P model parameters of nitrogen in Eq. S15.

	d_{11}	d_{12}	d_{13}	d_{14}
d_{11}	$1.766989254 \times 10^{-6}$	$\hbox{-}2.159150365{\times}10^{-6}$	$\text{-}5.574414865{\times}10^{-6}$	$-1.951006559 \times 10^{-6}$
d_{12}	$-2.159150365 \times 10^{-6}$	$1.247138092{\times}10^{-5}$	$1.446626083{\times}10^{-5}$	$3.785008465{\times}10^{-6}$
d_{13}	$-5.574414865 \times 10^{-6}$	$1.446626083\!\times\!10^{-5}$	$4.065416499{\times}10^{-5}$	$1.530007240\!\times\!10^{-5}$
d_{14}	$-1.951006559 \times 10^{-6}$	$3.785008465 \times 10^{-6}$	$1.530007240\!\times\!10^{-5}$	$6.186222625\!\times\!10^{-6}$

Table S6. The covariance matrix between the P- ρ model parameters of nitrogen in Eq. S16.

	d_{21}	d_{22}	d_{23}	d_{24}	d_{25}	d_{26}	d_{27}
d_{21}	$d_{21} = \frac{1.727107607 \times 10^4}{1.727107607 \times 10^4} + \frac{1.012363715 \times 10^5}{1.22606768 \times 10^5} + \frac{3.455338095 \times 10^4}{3.455338095 \times 10^4} + \frac{1.420484068 \times 10^3}{1.420484068 \times 10^3} + \frac{5.520946116 \times 10^5}{1.420484068 \times 10^3} + \frac{3.455338095 \times 10^4}{1.420484068 \times 10^3} + \frac{3.455338095}{1.420484068 \times 10^3} + \frac{3.455338095 \times 10^4}{1.420484068 \times 10^4} + \frac{3.45538095 \times 10^4}{1.42$	1.012363715×10^{5}	-3.272606768×10^4	3.455338095×10^4	$-1.420484068 \times 10^{3}$	5.520946116×10^{5}	-9.899038150×10^4
d_{22}		$3.806873493{\times}10^{6}$	$-1.908281102 \times 10^{5}$	$2.482284388{\times}10^{5}$	$1.012363715\times10^{5} - 3.806873493\times10^{6} - 1.908281102\times10^{5} - 2.482284388\times10^{5} - 6.482274999\times10^{5} - 4.078467118\times10^{6} - 8.039094772\times10^{5}$	$4.078467118 \times 10^{6}$	$-8.039094772 \times 10^{5}$
d_{23}		$-1.908281102 \times 10^{5}$	$6.201333234{\times}10^4$	$-6.546344263{\times}10^4$	$-3.272606768\times10^{4} - 1.908281102\times10^{5} - 6.201333234\times10^{4} - 6.546344263\times10^{4} - 2.691597031\times10^{3} - 1.045466672\times10^{4} - 1.874915558\times10^{3}$	-1.045466672×10^4	$1.874915558 \times 10^{3}$
d_{24}		$2.482284388{\times}10^{5}$	$-6.546344263{\times}10^4$	7.651077867×10^4	$3.455338095\times 10^{4} - 2.482284388\times 10^{5} - 6.546344263\times 10^{4} - 7.651077867\times 10^{4} - 2.705323473\times 10^{3} - 9.386355717\times 10^{5} - 2.106464904\times 10^{3}$	$9.386355717 \times 10^{5}$	$-2.106464904 \times 10^{3}$
d_{25}	$d_{25} = \begin{vmatrix} -1.420484068 \times 10^3 & -6.482274999 \times 10^5 & 2.691597031 \times 10^3 & -2.705323473 \times 10^3 & 1.198825559 \times 10^2 & -4.809804254 \times 10^4 & 7.859362901 \times 10^3 & 1.00000000000000000000000000000000000$	$-6.482274999 \times 10^{5}$	$2.691597031{\times}10^{3}$	-2.705323473×10^3	$1.198825559{\times}10^{2}$	-4.809804254×10^4	7.859362901×10^3
d_{26}	$5.520946116 \times 10^{5}$	$4.078467118 \times 10^{6}$	-1.045466672×10^4	$9.386355717 \times 10^{5}$	$5.520946116\times10^{5} - 4.078467118\times10^{6} - 1.045466672\times10^{4} - 9.386355717\times10^{5} - 4.809804254\times10^{4} - 2.321881450\times10^{5} - 2.966394393\times10^{4}$	$2.321881450{\times}10^{5}$	-2.966394393×10^4
d_{27}	$d_{27} = \begin{vmatrix} -9.899038150 \times 10^4 & -8.039094772 \times 10^5 & 1.874915558 \times 10^3 & -2.106464904 \times 10^3 & 7.859362901 \times 10^3 & -2.966394393 \times 10^4 & 5.964705514 \times 10^3 & 1.874915558 \times 10^4 & 1.874915558 \times 10^3 & -2.966394393 \times 10^4 & 1.874915558 \times 10^3 & -2.966394393 \times 10^4 & 1.874915558 \times 10^3 & -2.9664904 \times 10^3 & 1.874916 \times 10^3 & 1.87$	$-8.039094772 \times 10^{5}$	$1.874915558{\times}10^{3}$	$-2.106464904 \times 10^{3}$	$7.859362901{\times}10^{3}$	-2.966394393×10^4	$5.964705514 \times 10^{3}$

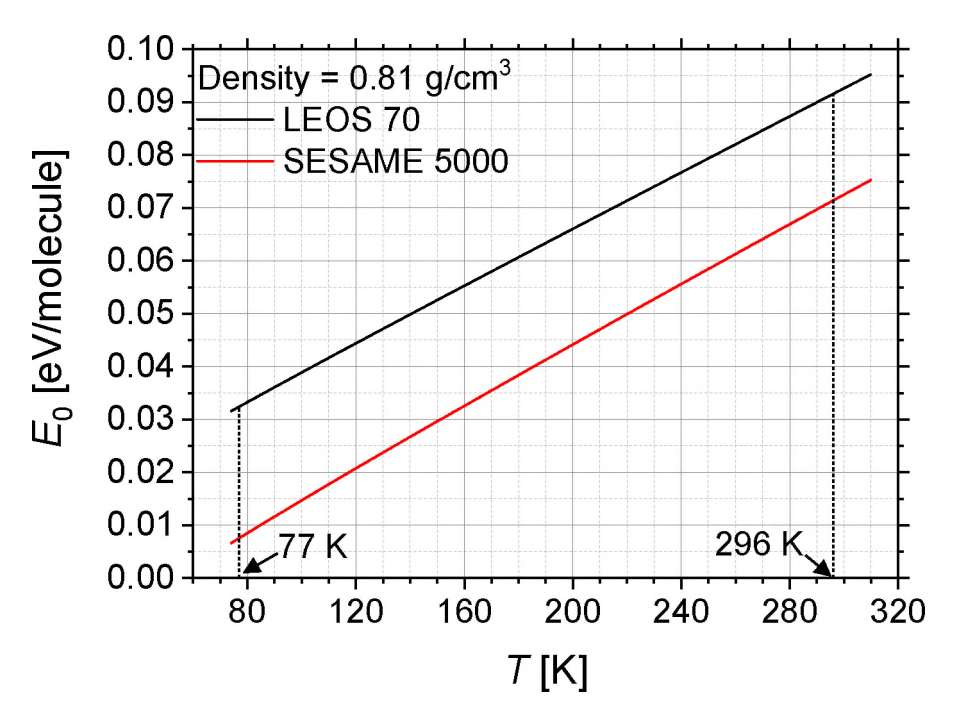


Figure S2. Internal energy (E_0) of molecular fluid nitrogen is computed along the isochore at 0.81 g/cm^3 with increasing temperature using LEOS 70 and SESAME 5000 models. Despite the different temperature (and pressure) conditions of cryogenic and precompressed samples, their internal energies are similar as 0.032 and 0.092 eV/molecule for LEOS 70 and 0.008 and 0.071 eV/molecule for SESAME 5000 at 77 (in literature) and 296 K (in this study), respectively. Their difference (0.060 and 0.063 eV/molecule for LEOS 70 and SESAME 5000, respectively) is almost negligible compared to a shock-induced internal energy variation $(E - E_0)$ which is 5-100 eV/molecule as shown in Fig. S1.

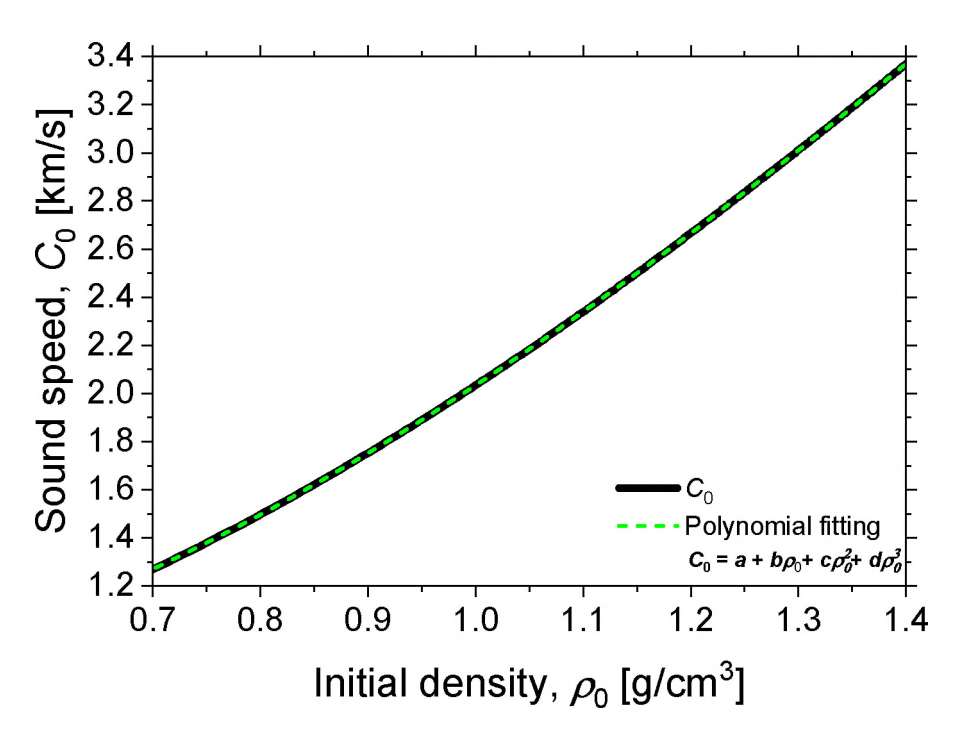


Figure S3. The measured shock velocity U_S is shifted from the initial density in this study (ρ_0 =0.76-1.29 g/cm³) to that of cryogenic nitrogen (ρ_{LN} =0.808 g/cm³ at 77 K). To find the U_S - ρ_0 relation, we use the empirical shock analysis framework where the shock velocity is often found to follow $U_S = C_0 + su_p$ where C_0 is the ambient sound speed. The C_0 - ρ_0 relation is inferred from previous studies [S5, S9] (thick black curve), and fitted with the third-order polynomial function (green dashed curve) between 0.7 and 1.4 g/cm³; $C_0(\rho_0) = a + b\rho_0 + c\rho_0^2 + d\rho_0^3$ where $a = 0.738 \pm 0.013$, $b = -0.815 \pm 0.038$, $c = 2.58 \pm 0.04$, and $d = -0.466 \pm 0.011$. The correction term is obtained as $\alpha_{Corr}(\rho_0) = C_0(\rho_{LN}) - C_0(\rho_0)$. Then, the shock velocity is corrected by adding this term; $U_{S.Corr}(\rho_{LN}) = U_S(\rho_0) + \alpha_{Corr}(\rho_0)$.

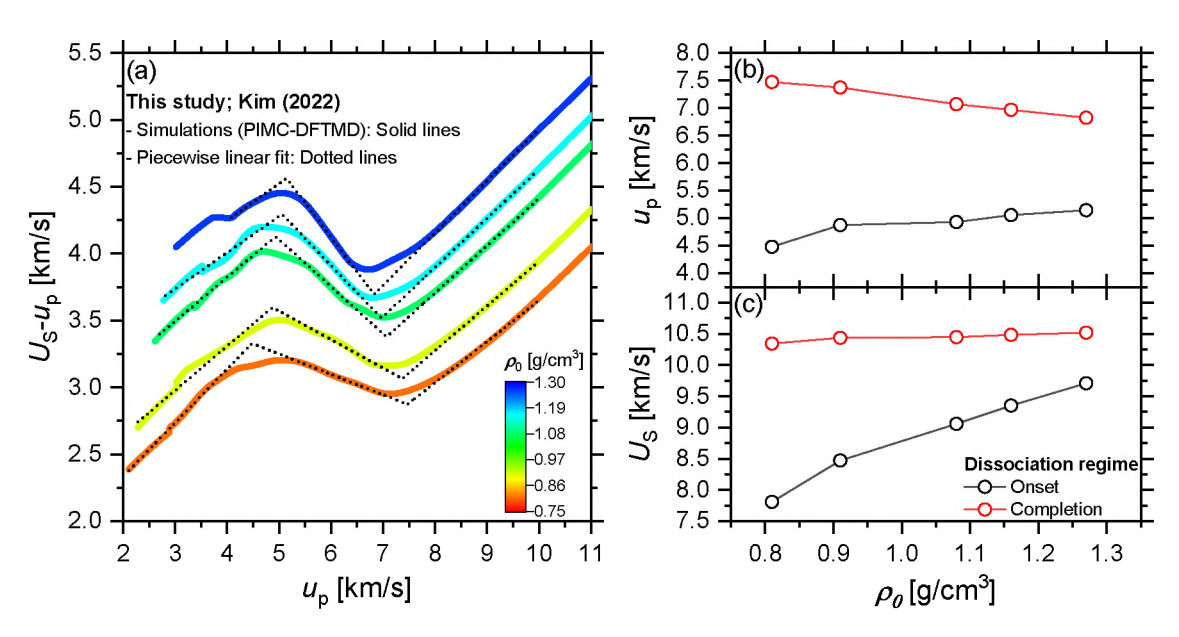


Figure S4. (a) Three-segment piecewise linear fitting is applied to our simulated Hugoniot curves between $u_p=2$ and 10 km/s to find inflection points that are related to the onset and completion of the molecular dissociation regime. (b and c) The u_p and U_s values of the inflection points (or the intersections of linear fits) are plotted as a function of the initial density. These plots reveal subtle trends pointing towards a more abrupt transition at the lower temperature and higher pressure conditions explored by the higher precompression curves (see Fig. S5).

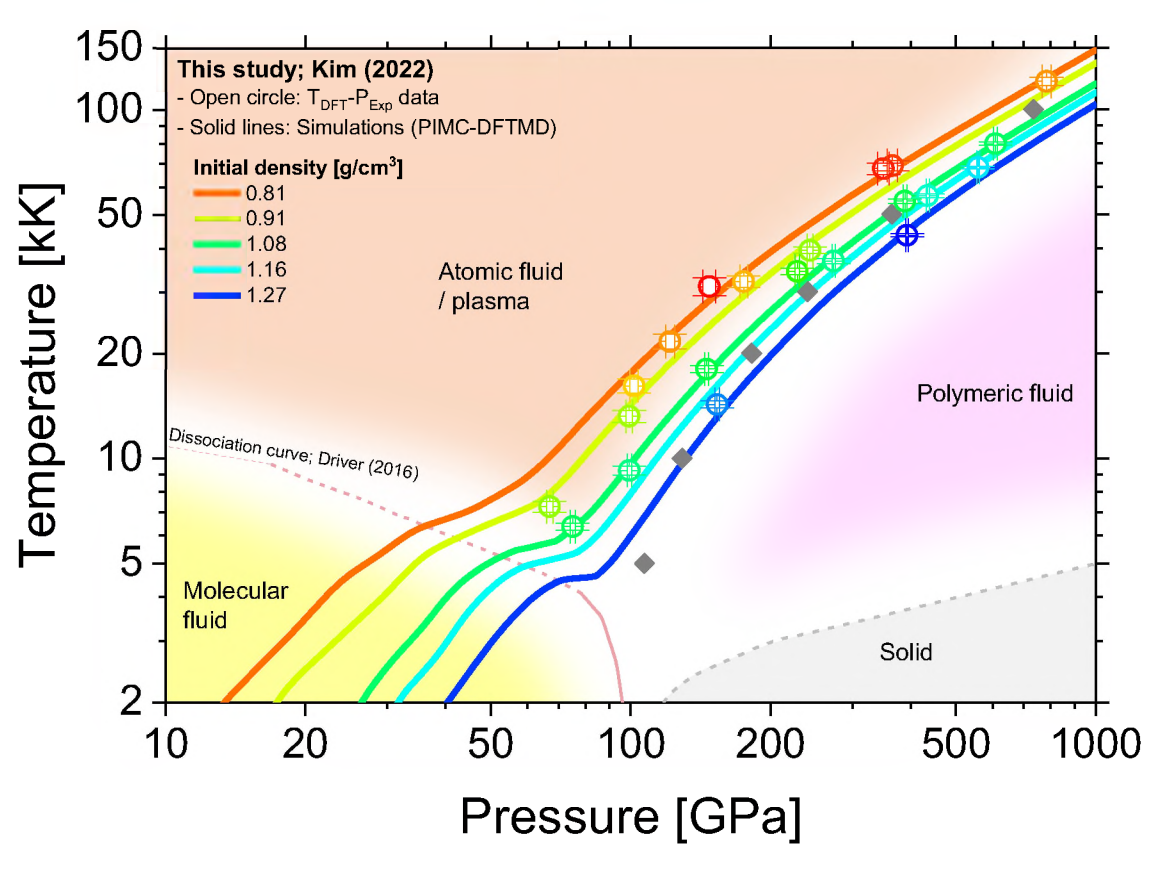


Figure S5. Temperature versus pressure phase diagram of nitrogen in the warm dense region. The experimental pressure vs computed temperature data (P and T_{DFT} in Table S2; open circle) and simulated Hugoniot curves (thick solid lines) starting from five different initial densities are overlain on the phase diagram of Driver and Militzer [S31], showing solid [S31, S32] and fluid phases and plasma regime. The curves tend to shift toward a cooler but denser region with increasing initial density. Along the simulated curves, the molecular nitrogen fluid is dissociated into atomic fluid [S31] and ionized to the plasma phase rather than forming polymeric [S24, S33] or metallic [S34] fluids. The dissociation boundary (thick pink dashed curve) is derived from DFTMD simulations [S31], and becomes the first-order transition at lower temperature and higher pressure (thick pink solid curve), inducing a sharper dissociation with increasing initial density as observed at $5 < u_p < 8$ km/s in Fig. 2c in the main text. We note that the microscopic structure of the dissociated nitrogen could be more complicated than a simple single atomic fluid, especially in our highest-initial-density data for which the simulated Hugoniot curve (thick blue) is close to the atomic-polymeric fluid boundary. The gray diamonds show the six points at a constant density of 3.706 g/cc for which the electronic density of states is shown in Fig. S9.

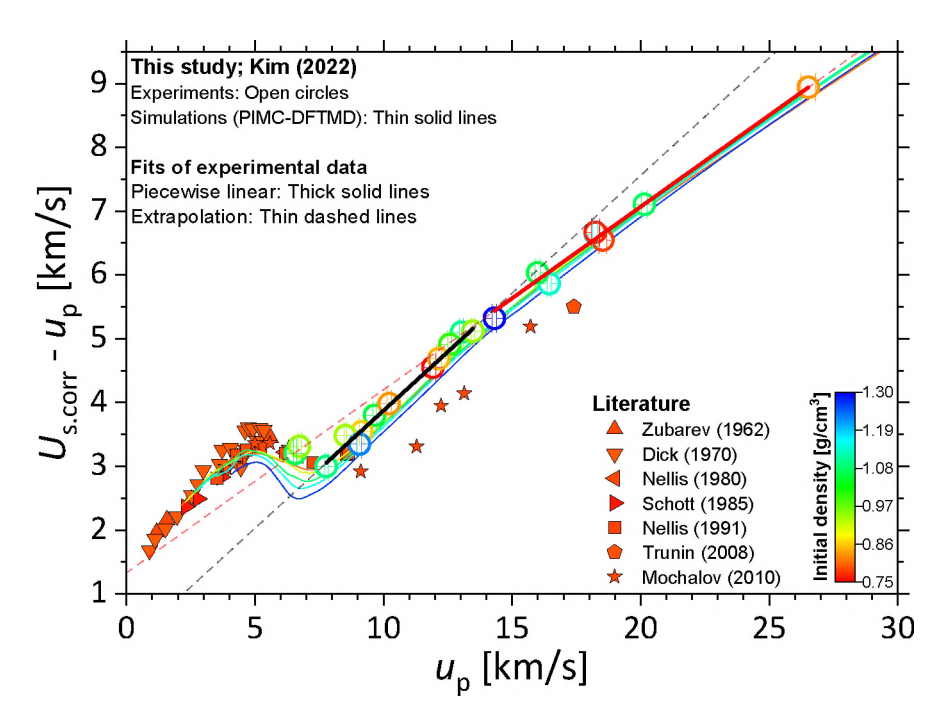


Figure S6. Two-segment piecewise linear fitting $(U_{S.Corr} = a + bu_p)$ is applied to our experimental data $(u_p = 7.77 - 26.52 \text{ km/s})$. We find the fitting parameters of $a_1 = 0.19 \pm 0.15 \text{ km/s}$ and $b_1 = 1.37 \pm 0.01$ at $u_p = 7.77 - 13.47 \text{ km/s}$ (thick black solid line), and $a_2 = 1.33 \pm 0.16 \text{ km/s}$ and $b_2 = 1.29 \pm 0.01$ at $u_p = 14.31 - 26.52 \text{ km/s}$ with a slightly lower slope (thick red solid line). This piecewise fitting provides a slope discontinuity near $u_p = 14 \text{ km/s}$, a signature of the onset of L-shell ionization of dissociated atomic fluid. Statistical analyses using Akaike and Bayesian information criteria (AIC and BIC) tests and a F-test indicate that the piecewise model is a better representation of the experimental data than a linear model.

Uncertainties in hemispherical impact experiments

Hemispherical-explosive impact experiments by Trunin et al. [S23] and Mochalov et al. [S24] provided Hugoniot data points at 88-320 GPa, beyond the shock-induced chemical dissociation of molecular nitrogen. However, compared to our new data and previous experimental [S18, S22] and simulation [S31] results, they reported slower shock velocity and denser shock states (see Figs. 2b and 3a in the main text). To elucidate whether this discrepant behavior of shock-compressed nitrogen was arising from the use of different shock standards (aluminum and iron), we computed the impedance matching results for the four data points from Ref. [S24] having an Al reference using the model from Ref. [S35] which has been found to be consistent with our quartz model.

We focus on the four experiments using an aluminum reference (1_MZ-4 SWG, 2_MZ-8 SWG, 4_MZ-13 SWG, and 5_MZ-8 SWG) in Ref. [S24]. The reported shock parameters are summarized in Table. S7; $U_{S,Al}^{meas}$ and U_{S}^{meas} are the measured shock velocity of the aluminum impactor and nitrogen sample, obtained from the transit time through each hemispherical layer; $U_{S,Al}^{sim}$ is the shock velocity of aluminum corrected for the expected velocity increase due to the spherical convergence by comparing with 1D hydrodynamic simulations; and u_p , P, and ρ are the particle velocity, pressure, and density of shock-compressed nitrogen.

As the uncertainties for all $U_{S,Al}^{sim}$ were not reported [S24], they are evaluated from those of $U_{S,Al}^{meas}$. For the first two shots (1_MZ-4 SWG and 2_MZ-8 SWG), we assume that the uncertainty is proportional to the shock velocity;

$$U_{S,Al.err}^{sim} = U_{S,Al.err}^{meas}(U_{S,Al}^{sim}/U_{S,Al}^{meas}), \tag{S17}$$

where $U_{S,Al.err}^{sim}$ and $U_{S,Al.err}^{meas}$ are the uncertainties in $U_{S,Al}^{sim}$ and $U_{S,Al.err}^{meas}$. Due to the lack of $U_{S,Al}^{meas}$ values for the last two shots (4_MZ-13 SWG and 5_MZ-8 SWG), their $U_{S,Al.err}^{sim}$ are approximated using the values of the second shot (2_MZ-8 SWG);

$$U_{S,Al.err}^{sim} = 14.91(U_{S,Al}^{sim}/0.71).$$
 (S18)

Table S7. Shot numbers and shock parameters reported by Mochalov et al. [S24] for hemispherical impacts and re-analyzed in this study. Uncertainties on $U_{S,Al}^{sim}$ are assessed with Eqs. S17 and S18. Initial densities of aluminum impactor and nitrogen sample are 2.742 and 0.807 g/cm³ [S24].

		Shock p	arameters in	Ref. [S	24]		Reanalyzed results		
Shot number	$U_{S,Al}^{meas}$	$U_{S,Al}^{sim}$	U_S^{meas}	u_p	P	ρ	u_p'	P'	ρ'
	[km/s]	$[\mathrm{km/s}]$	$[\mathrm{km/s}]$	[km/s]	[GPa]	$[g/cm^3]$	$[\mathrm{km/s}]$	[GPa]	$[g/cm^3]$
1_MZ-4 SWG	12.74±0.42	13.55 ± 0.45	12.03±0.25	9.11	88.4±2	3.33±0.20	9.03±0.55	87.8±5.4	3.24 ± 0.59
2_MZ -8 SWG	14.91±0.71	16.49±0.79	16.19±0.36	12.24	160 ± 3	3.31 ± 0.26	12.27±1.11	161 ± 15	3.34 ± 0.95
4 _ MZ - $13~SWG$	-	19.70±0.94	20.90±0.68	15.71	265 ± 5	3.25 ± 0.25	15.76 ± 1.28	266 ± 22	3.28 ± 0.82
5_MZ-8 SWG	-	17.31±0.82	17.28 ± 0.40	13.14	183±6	3.37±0.35	13.19±1.14	184±16	3.41 ± 0.96

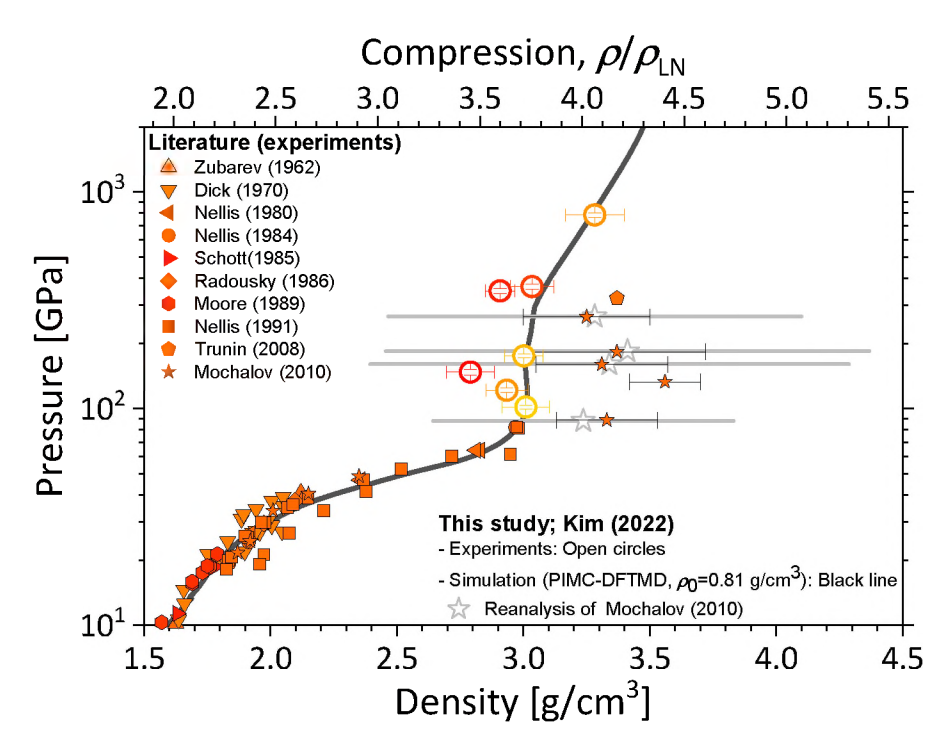


Figure S7. Pressure versus density of nitrogen for our low initial-density data (ρ_0 =0.760–0.87 g/cm³) (open circle) and previous [S15–S24] studies (closed symbols) with calculated Hugoniot curves using the PIMC-DFMD simulation (thick black curve) for 0.81 g/cm³ nitrogen, as shown in Fig. 3a in the main text. When the results of hemispherical impacts by Mochalov et al. [S24] (closed star) are reanalyzed (gray open star), the uncertainties on the inferred shock density (thick gray line) are 2.7-3.7 times larger than the original values (thin black line) and agree with our data.

With $U_{S,Al}^{sim}$, U_S^{meas} and the re-evaluated uncertainty on $U_{S,Al}^{sim}$, we calculate the particle velocity, shock pressure, and shock density $(u_p', P', \text{ and } \rho')$ following the framework described by Celliers *et al.* [S35], including analytical error propagation. We note that one shot in Ref. [S23] and one shot with a steel impactor (3_MZ-8 SWG) in Ref. [S24] are not reanalyzed here because of the absences of error information and a model similar to Ref. [S35] for a steel reference.

The results are summarized and compared with the original analysis [S24] in Table. S7 and Fig. S7. The inferred pressure-density results from this analysis are consistent within 3 % with the original study. However, we find that the reported large velocity uncertainty leads to much larger shock density uncertainty than those reported in Ref. [S24]. The uncertainties on the inferred density (0.59-0.96 g/cm³) are 2.7-3.7 times larger than those initially reported (0.20-0.35 g/cm³). Indeed, plotting the results of this re-analysis (Fig. S7) reveals that the larger error bars for the data of Ref. [S24] now overlap with our result, therefore relieving the statistical discrepancy between the two studies. We note that the re-analyzed uncertainties are mostly contributed by a random uncertainty (96-99 %) rather than a systematic one (15-29 %), and the later is close with the original values.

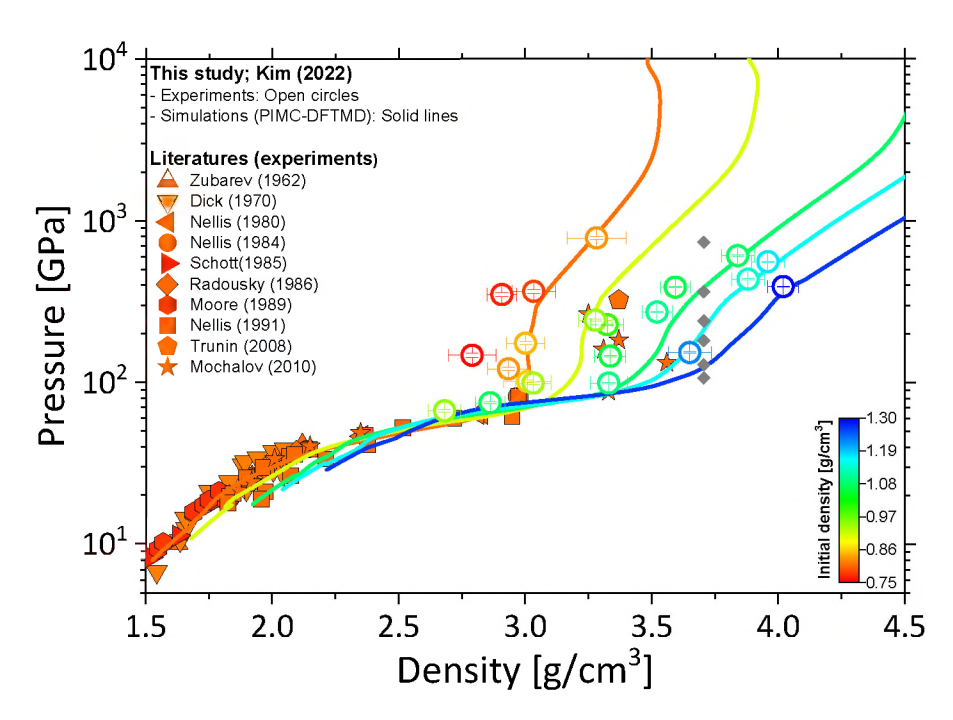


Figure S8. Shock pressure versus density data. Color scale representing sample's initial density is used for both experimental data and calculated Hugoniot curves. The gray diamonds show the six points at a constant density of 3.706 g/cc for which the electronic density of states is shown in Fig. S9.

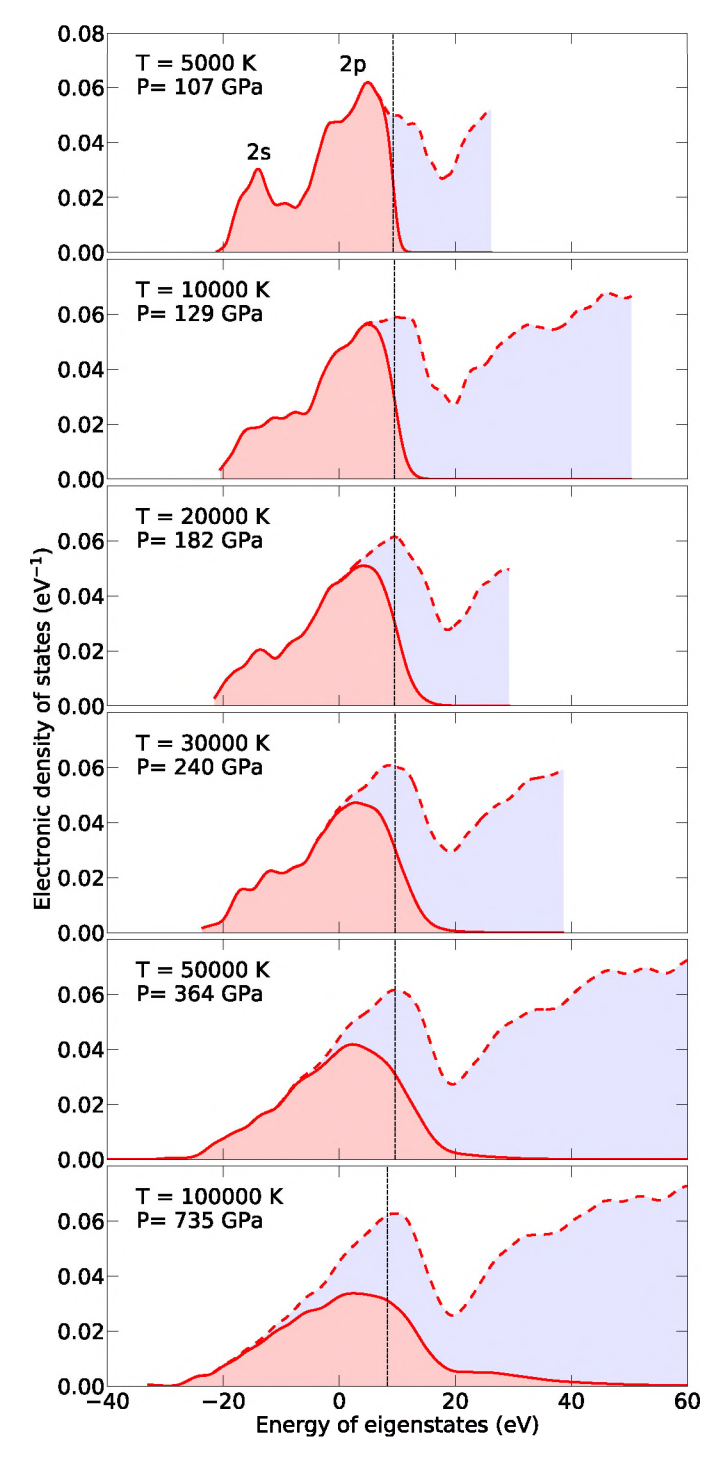


Figure S9. Electronic density of states computed with DFTMD simulations at various pressure-temperature conditions for a density of 3.706 g/cc. The pressure-density-temperature states for the simulations are indicated with gray diamonds in Figs. S5 and S8. The solid lines show the density of the occupied electronic states while the dashed lines represent all available states. At low pressure (and temperature), the L-shell is almost completely occupied and the 2s and 2p peaks can be distinguished. That distinction gradually disappears with increasing pressure (and temperature), as more and more electrons become excited and occupy states above the Fermi energy that is indicated by the vertical dashed lines. These electronic excitations increase the internal energy, which leads to an increase in shock compression as is discussed by Militzer [S36].

- [S1] G. Ghosh, Dispersion-equation coefficients for the refractive index and birefringence of calcite and quartz crystals, Optics Communications 163, 95 (1999).
- [S2] E. Calderon, M. Gauthier, F. Decremps, G. Hamel, G. Syfosse, and A. Polian, Complete determination of the elastic moduli of α-quartz under hydrostatic pressure up to 1 GPa: an ultrasonic study, Journal of Physics: Condensed Matter 19, 436228 (2007).
- [S3] H. Kimizuka, S. Ogata, J. Li, and Y. Shibutani, Complete set of elastic constants of α-quartz at high pressure: A first-principles study, Physical Review B 75, 054109 (2007).
- [S4] S. Brygoo, M. Millot, P. Loubeyre, A. E. Lazicki, S. Hamel, T. Qi, P. M. Celliers, F. Coppari, J. H. Eggert, D. E. Fratanduono, D. G. Hicks, J. R. Rygg, R. F. Smith, D. C. Swift, G. W. Collins, and R. Jeanloz, Analysis of laser shock experiments on precompressed samples using a quartz reference and application to warm dense hydrogen and helium, Journal of Applied Physics 118, 195901 (2015).
- [S5] R. L. Mills, D. H. Liebenberg, and J. C. Bronson, Sound velocity and the equation of state of N₂ to 22 kbar, The Journal of Chemical Physics 63, 1198 (1975).
- [S6] D. Fabre and B. Oksengorn, Pressure and Density Dependence of the CH₄ and N₂ Raman Lines in an Equimolar CH₄/N₂ Gas Mixture, Applied Spectroscopy **46**, 468 (1992).
- [S7] H. D. Hochheimer, K. Weishaupt, and M. Takesada, High-pressure Brillouin scattering study of dense argon and nitrogen, The Journal of Chemical Physics 105, 374 (1996).
- [S8] S. Jiang, N. Holtgrewe, S. S. Lobanov, F. Su, M. F. Mahmood, R. S. McWilliams, and A. F. Goncharov, Metallization and molecular dissociation of dense fluid nitrogen, Nature Communications 9, 2624 (2018).
- [S9] S. Ninet, G. Weck, A. Dewaele, F. Datchi, V. M. Giordano, and P. Loubeyre, Sound velocity and refractive index of pure N₂ fluid and of equimolar N₂-CO₂ fluid mixture up to 15 GPa, The Journal of Chemical Physics 153, 114503 (2020).
- [S10] P. M. Celliers, D. K. Bradley, G. W. Collins, D. G. Hicks, T. R. Boehly, and W. J. Armstrong, Line-imaging velocimeter for shock diagnostics at the OMEGA laser facility, Review of Scientific Instruments 75, 4916 (2004).
- [S11] M. Millot, S. Hamel, J. R. Rygg, P. M. Celliers, G. W. Collins, F. Coppari, D. E. Fratanduono, R. Jeanloz, D. C. Swift, and J. H. Eggert, Experimental evidence for superionic water ice using shock compression, Nature Physics 14, 297 (2018).
- [S12] Y.-J. Kim, P. M. Celliers, J. H. Eggert, A. Lazicki, and M. Millot, Interferometric measurements of refractive index and dispersion at high pressure, Scientific Reports 11, 5610 (2021).
- [S13] D. G. Hicks, T. R. Boehly, P. M. Celliers, J. H. Eggert, S. J. Moon, D. D. Meyerhofer, and G. W. Collins, Laser-driven single shock compression of fluid deuterium from 45 to 220 GPa, Physical Review B 79, 014112 (2009).
- [S14] B. Militzer, F. González-Cataldo, S. Zhang, K. P. Driver, and F. Soubiran, First-principles equation of state database for warm dense matter computation, *Physical Review E* **103**, 013203 (2021).
- [S15] V. Zubarev, Impact compressibility of liquid nitrogen and solid carbon dioxide, Dokl. Akad. Nauk SSSR 142, 309 (1962).
- [S16] R. D. Dick, Shock Wave Compression of Benzene, Carbon Disulfide, Carbon Tetrachloride, and Liquid Nitrogen, The Journal of Chemical Physics 52, 6021 (1970).
- [S17] W. J. Nellis and A. C. Mitchell, Shock compression of liquid argon, nitrogen, and oxygen to 90 GPa (900 kbar),

- The Journal of Chemical Physics 73, 6137 (1980).
- [S18] W. J. Nellis, N. C. Holmes, A. C. Mitchell, and M. van Thiel, Phase Transition in Fluid Nitrogen at High Densities and Temperatures, Physical Review Letters 53, 1661 (1984).
- [S19] G. L. Schott, M. S. Shaw, and J. D. Johnson, Shocked states from initially liquid oxygen-nitrogen systems, The Journal of Chemical Physics 82, 4264 (1985).
- [S20] H. B. Radousky, W. J. Nellis, M. Ross, D. C. Hamilton, and A. C. Mitchell, Molecular Dissociation and Shock-Induced Cooling in Fluid Nitrogen at High Densities and Temperatures, Physical Review Letters 57, 2419 (1986).
- [S21] D. S. Moore, S. C. Schmidt, M. S. Shaw, and J. D. Johnson, Coherent anti-Stokes Raman spectroscopy of shock-compressed liquid nitrogen, The Journal of Chemical Physics 90, 1368 (1989).
- [S22] W. J. Nellis, H. B. Radousky, D. C. Hamilton, A. C. Mitchell, N. C. Holmes, K. B. Christianson, and M. van Thiel, Equation-of-state, shock-temperature, and electrical-conductivity data of dense fluid nitrogen in the region of the dissociative phase transition, The Journal of Chemical Physics 94, 2244 (1991).
- [S23] R. F. Trunin, G. V. Boriskov, A. I. Bykov, A. B. Medvedev, G. V. Simakov, and A. N. Shuikin, Shock compression of liquid nitrogen at a pressure of 320 GPa, JETP Letters 88, 189 (2008).
- [S24] M. A. Mochalov, M. V. Zhernokletov, R. I. Il'kaev, A. L. Mikhailov, V. E. Fortov, V. K. Gryaznov, I. L. Iosilevskiy, A. B. Mezhevov, A. E. Kovalev, S. I. Kirshanov, Y. A. Grigor'eva, M. G. Novikov, and A. N. Shuikin, Measurement of density, temperature, and electrical conductivity of a shock-compressed nonideal nitrogen plasma in the megabar pressure range, Journal of Experimental and Theoretical Physics 110, 67 (2010).
- [S25] J. C. Chervin, B. Canny, and M. Mancinelli, Ruby-spheres as pressure gauge for optically transparent high pressure cells, High Pressure Research 21, 305 (2001).
- [S26] Y. B. Zeldovich and Y. P. Raizer, Physics of Shock Waves and High-Temperature Hydrodynamic Phenomena (Elsevier, 1967).
- [S27] M. P. Desjarlais, M. D. Knudson, and K. R. Cochrane, Extension of the Hugoniot and analytical release model of α-quartz to 0.2-3 TPa, Journal of Applied Physics 122, 035903 (2017).
- [S28] W. J. Moonan, Linear Transformation to a Set of Stochastically Dependent Normal Variables, Journal of the American Statistical Association 52, 247 (1957).
- [S29] R. Y. Rubinstein and D. P. Kroese, Simulation and the Monte Carlo Method, 3rd ed. (John Wiley & Sons, Inc., 2016).
- [S30] A.-L. Cholesky, Sur la résolution numérique des systèmes d'équations linéaires, Bulletin de la Sabix, 81 (2005).
- [S31] K. P. Driver and B. Militzer, First-principles equation of state calculations of warm dense nitrogen, Physical Review B 93, 064101 (2016).
- [S32] J. Sun, M. Martinez-Canales, D. D. Klug, C. J. Pickard, and R. J. Needs, Stable All-Nitrogen Metallic Salt at Terapascal Pressures, Physical Review Letters 111, 175502 (2013).
- [S33] M. Ross and F. Rogers, Polymerization, shock cooling, and the high-pressure phase diagram of nitrogen, Physical Review B 74, 024103 (2006).
- [S34] R. Chau, A. C. Mitchell, R. W. Minich, and W. J. Nellis, Metallization of Fluid Nitrogen and the Mott Transition in Highly Compressed Low-Z Fluids, Physical Review Letters 90, 245501 (2003).
- [S35] P. M. Celliers, G. W. Collins, D. G. Hicks, and J. H. Eggert, Systematic uncertainties in shock-wave impedance-match analysis and the high-pressure equation of state of Al, Journal of Applied Physics 98, 113529 (2005).

[S36] B. Militzer, First Principles Calculations of Shock Compressed Fluid Helium, Physical Review Letters 97, 175501 (2006).